Three-dimensional crack observation, quantification and simulation in a quasi-brittle material*

M. Mostafavi [1,#i], N. Baimpas [2], E. Tarleton [1], R. C. Atwood [3], S. A. McDonald [4], A. M. Korsunsky [2], T.J. Marrow [1,#]

[1] Department of Materials and [#] Oxford Martin School, University of Oxford

[2] Department of Engineering Science, University of Oxford

[3] Diamond Light Source, Harwell Science and Innovation Campus, Oxfordshire

[4] Manchester X-ray Imaging Facility, University of Manchester

Abstract

To investigate the fracture behaviour of polygranular graphite (a quasi-brittle material), crack propagation in a short bar chevron notched specimen was studied by synchrotron X-ray computed tomography combined with digital volume correlation

---

[i] Corresponding author: Mahmoud Mostafavi, Department of Mechanical Engineering, University of Sheffield, Sir Mappin Building, Mappin Street, Sheffield S1 3JD (m.mostafavi@sheffield.ac.uk)

(DVC). Displacements were measured within the loaded test specimen, particularly the three-dimensional profile of crack opening displacement. Analysis of the three-dimensional displacement field confirmed the existence of distributed damage in a fracture process zone, which significantly increased the effective crack length. Finite element simulations affirmed that the measured crack opening profiles could be reproduced using a cohesive zone model, but not with a linear elastic analysis. Comparing the simulation and experimental results, it was deduced that the critical strain energy release rate varied across the crack front; i.e. the fracture toughness is constraint-dependent. This is proposed to be a general characteristic of quasi-brittle materials.

1 Introduction

The structural integrity of quasi-brittle materials, such as graphite [1-3], ceramic composites [4] and bone and bone replacements [5], is commonly assessed with the conservative assumption of brittle fracture (e.g. [6, 7]). Although the nonlinear behaviour of some quasi-brittle materials such as concrete has received much attention in the fracture community (e.g. [8-10]), the inelastic behaviour of many quasi-brittle materials is generally treated as negligible (e.g. for graphite see [6, 11, 12]); yet post-initiation tension-softening behaviour can play an important role in the integrity of components that are made of quasi-brittle materials. Understanding and quantifying this effect could improve confidence in the safety margins of their structural integrity assessment.

During the fracture of a partially-cracked component that is fabricated from a quasi-brittle material, a fracture process zone develops due to distributed microcracking ahead of the crack tip [2, 13]. The extent of the fracture process zone dictates the magnitude of the deviation of the component's deformation and fracture behaviour from that predicted by linear elastic analysis. An analogy may be established between the fracture process zone in quasi-brittle materials and the plastic zone in ductile materials [14]: a larger fracture process zone contributes more redundant inelastic energy to the measured critical energy release rate, resulting in higher fracture resistance. The fracture process zone can increase in size with crack propagation [15], leading to the classic R-curve behaviour [16]. In-plane constraint (geometric)

and out-of-plane constraint (thickness) influence the fracture of elastic-plastic materials [17-19], and it is therefore likely that quasi-brittle materials are similarly affected [20].

In-plane constraint effects have been studied in polygranular graphites through the sensitivity of their R-curve to stress state [21] and geometry [22]. Although indications of out-of-plane constraint effects, such as crack tunnelling [23], have been also also observed, it has not been investigated fully. An objective of the study reported in this paper is therefore to examine through-thickness variation of the crack propagation behaviour in graphite. Measurements of the three-dimensional displacements in a cracked specimen can provide useful information on fracture behaviour, as demonstrated in recent combined X-ray computed tomography (XCT) and digital volume correlation (DVC) studies [21, 24], in which full-field displacement measurements were used to map the three-dimensional crack opening profile. The measurements allow testing of the validity of crack opening profile simulations, obtained by the finite element method for different material models.

It has been well established that there is a fundamental difference between the crack opening profiles obtained by models that consider the strip yield model, and the predictions of linear elastic or elastic-plastic fracture mechanics [25, 26] (schematic profiles are compared in Figure 1a). A recent investigation in polygranular graphite [24] showed that the measured crack opening profile was close to that suggested by strip yield models. Crack propagation in materials that demonstrate strip yield model behaviour [27] may be simulated by cohesive zone modelling. Proposed by Hillerborg, Modeer and Petersson [8] through a traction-separation law (Figure 1b), cohesive zone models have been applied widely, simulating fracture in concrete (for example [9, 28-31]), adhesively bonded joints [32, 33], ceramic-metal composites [34] and elastic-plastic ductile metals [20, 35]. The fracture process in quasi-brittle materials other than concrete, such as bone [36] and graphite [37], has also been simulated by cohesive zone models.

Gilsocarbon is a near-isotropic, heterogeneous artificial graphite used in UK's advanced gas cooled (AGR) nuclear fission reactors as moderator and reflector, which are load-bearing components [38] in the form of graphite blocks that are keyed in a structure that forms the reactor core. Dimensional change of the graphite, caused by

fast neutron irradiation and thermal strains, develops multi-axial stresses within the structure; these have the potential to initiate fracture in the moderator blocks [39]. Improved understanding and knowledge of the criteria for crack initiation and propagation in graphite under different constraint conditions, both in-plane (i.e. geometry and stress-states) and out-of-plane (i.e. through thickness) can support the integrity assessment of the graphite bricks. It has been shown for materials with elastic-plastic behaviour that taking constraint into account can reduce over-conservatism in fracture assessments, allowing the life of components to be safely extended [40]. It is therefore useful to develop an analogous treatment of quasi-brittle materials that can support the assessment of graphite components.

Small samples are extracted from the core of operating reactors to monitor changes in the properties of the graphite. Though not presently used to measure fracture properties, other than flexural strength, the size of such extracted samples may be suitable to fabricate test specimens to study fracture behaviour [41, 42]. To investigate the potential of such tests, crack initiation and propagation were examined in this work using a chevron notch specimen fabricated from 'virgin' (un-irradiated) Gilsocarbon graphite. X-ray tomographic images were taken of the specimen in its un-damaged condition at Diamond Light Source synchrotron (beamline I12). A sharp wedge was driven progressively into the specimen's notch to initiate and propagate a crack; tomographic images were taken at each loading stage and subsequently analysed using commercially available digital volume correlation software [43] to obtain full-field three-dimensional displacements, thereby measuring the crack opening profile. Digital Image Correlation (DIC) analysis [44, 45] has become a routine tool to study the deformation, fatigue and fracture behaviour of materials by analysis of two-dimensional images (e.g. see [46-51]). Digital volume correlation (DVC) is based on a similar mathematical concept, extended to three dimensions [52-54].

The improved measurement precision in this work, relative to an earlier low-resolution laboratory tomography study [21, 24] allows cohesive zone models and their input parameters to be tested by experimental data. A strip-yield model of the crack opening was simulated using Abaqus/standard V. 6.10 [55] employing the cohesive zone modelling technique [56] through a cohesive contact model. A bilinear

traction separation law (Figure 1b) was used to describe the cohesive properties, taking its parameters from extant uniaxial strength and high constraint fracture toughness data [23, 57], as suggested by Cornec, Scheider and Schwalbe [58]. The observations show that the crack opening behaviour across the crack front cannot be simulated using a constant set of material parameters, indicating that the cohesive energy (i.e. the fracture resistance) of quasi-brittle materials is constraint dependent, similar to elastic-plastic materials [35].

2 Experiment

2.1 Specimen geometry and loading

The short bar chevron notch specimen was designed following the recommendations of the International Society of Rock Mechanics [42]. The geometry of the specimen is shown in Figure 2a, and its dimensions are reported in Table 1. The crack is initiated and propagated by carefully driving a wedge into the notch, causing the two sides of the specimen to open. The coordinate system used throughout this paper, for a crack of length a, is depicted in Figure 2b. One end of the specimen was threaded for fixing into the loading rig; this is shown in Figure 2a, denoted by T, but is removed from the schematics hereafter for clarity.

The specimen was scanned in its as-received condition (loading sequence 0) and then loaded until a maximum load of 310 N was achieved (loading sequence A). The load on the wedge was reduced to zero by progressively withdrawing the wedge (loading sequence C). The specimen was then loaded progressively to 360 N (loading sequence G). Intermediate scans were performed (sequences D to F), but are not reported here in detail. The loading sequence is summarised in Table 2. Inspection of the tomographic reconstructions identified a macroscopic crack that was approximately 3.4 mm in loading sequence A, which propagated to a length of 3.7 mm by loading sequence G (see section 2.2). The macroscopic crack wake (i.e. the material behind the crack tip) was removed using electro-discharge machining up to a position within ±0.2 mm of the identified crack tip, and the final scan was recorded (loading sequence H).

2.2 X-ray computed tomography

Absorption contrast X-ray computed tomography was performed at the Diamond Light Source, Joint Engineering, Environmental and Processing beamline (I12 – JEEP) in the UK. In-situ loading was carried out with a compression rig equipped with a Plexiglas tube, transparent to visible and X-ray light. The loading rig (manufactured by 'DEBEN') is shown in Figure 2c on the I12 stage. The beam was monochromated at 80 keV using a double crystal Si monochromator; 4500 projections over 180° were recorded (i.e. at 0.04° rotation increments) with the specimen rotating around an axis parallel to the *z* direction (Figure 2b). A high resolution imaging detector (PCO.4000) was used for data acquisition. The detector field of view is 4000×2672 pixels (*x*×*z*), with two adjustable scintillator-objective sets at different magnifications used to record the projections: standard resolution (denoted by SR) with voxel size ~5 μm and high resolution (denoted by HR) with voxel size ~1.8 μm. The SR scans allowed an area of 20×13.4 mm^2 to be radiographer. The HR scans, although observing a smaller area (7.2×4.8 mm^2) provided better microstructural observations. Table 2 summarises the magnification used at each loading sequence. The exposure times were 2 seconds and 3 seconds for the SR and HR scans respectively, with an extra second required for the data transfer. The time per tomography scan was therefore four hours for SR and five hours for HR observations.

High-resolution computed X-ray tomography requires subtraction of a 'flat-field' image (i.e. no sample in the field of view) from each projection image in order to remove the effects that arise due to the variations in detector sensitivity. It is common practice to use a single flat field image to correct all projections, particularly when the scan time is short. However, the Perspex tube had two slots so that environmental data (such as temperature) might be recorded while performing XCT scans through sensors attached to specimens. Although no sensors were used in this experiment, the slots were unavoidably present in the field of view of the test specimen, resulting in the variations in the flat field image. To obtain individual flat-field images and thus to correct for the effects of the slots and other physical marks on the Perspex tube, a tomography scan of the empty tube was performed.

An in-house sinogram generation and filtered back-projection reconstruction MATLAB® implemented algorithm was used. The sinogram generation procedure

used the combined wavelet-Fourier filtering ring artefact removal technique introduced by Munch and co-workers [59]. For reference, the best results were obtained with a global DB10 wavelet filter, with parameters L=8 and σ=6, where L is the highest decomposition level of the multi-scale wavelet transform and σ is width of the filter in the FFT (Fast Fourier Transform) for vertical strip removal. A finer artefact removal approach with a DB10 wavelet filter, L=6 and σ=6 was performed at the central region of the sinograms (120 pixels wide). A dark-field image (i.e. detector output with no X-ray beam) was subtracted from each projection and a generated flat-field sinograms were used for better contrast. Finally, an intensity equilibration filter was used to counteract the flux variation during the synchrotron ring top-up periods. Anti-speckle filtering was applied at the sinograms and median filtering was performed on the reconstructed images [4x4 window size]. Each scan provided 2672 virtual slices in the form of 4008×4008 (horizontal resolution of the detector) pixel 16-bit images separated by the vertical resolution of the detector. Figure 3a shows the virtual slices with respect to the specimen. Reconstructions were afterwards converted to 8-bit raw stacks to be the input for the DVC calculation.

Examples of HR virtual slices (2.1 mm below the tip of the notch) in the un-cracked (i.e. the reference state) states are shown in Figure 3b, and 3c without and with the combined wavelet Fourier filtering ring artefact removal applied respectively; the rings are concentric about the centre of rotation. Figure 3c shows that the rings are successfully suppressed but there is a local artefact (identified by dashed box) at the centre of the rotation, arising from the wavelet-Fourier filtering ring artefact removal algorithm. Figure 3d shows the same virtual slice as Figure 3a and Figure 3b, after the specimen is cracked (with combined wavelet-Fourier filtering ring artefact removal). SR virtual slices at the same position (Figure 3e and f) show the crack less visibly; the crack is difficult to resolve due to its small opening displacement; the absorption contrast of the open crack is also similar to that of the porosity, which makes data segmentation to visualise the crack extremely difficult. Visual observations of the crack tip position (see Table 3 for details) show no significant difference between SR and HR observations, the HR measurement being slightly greater than the SR by less than 50 μm. The crack length increased from about 3.4 mm to 3.7 mm through the course of the experiment.

3 Digital volume correlation analysis

Digital volume correlation analyses were performed on the tomography datasets, using Davis Strain Master software (Version 8.1) [43]. Each was correlated against the as-received condition (loading cycle 0) with a 256×256×256 interrogation window, 50% overlap and 2 passes, followed by 64×64×64 interrogation window, 50% overlap, 2 passes and finally followed by 32×32×32 interrogation window, 50% overlap and 4 passes. Examples of the displacement fields (V_y) are presented in Figure 4a and b, at the approximate position of the virtual slices shown in Figure 3 for the HR and SR scans respectively; due to the size of the interrogation window with 50% overlap in the analysis, the displacement field slice represents material within ±16 voxels of the absorption tomography slice, which is equivalent to ±0.03 mm for HR and ±0.08 mm for SR. The white patches in the figures indicate the areas where the displacement vectors were deleted due to a low coefficient of correlation (<0.5), attributed to effects of image noise and artefacts. The figures show a clear step in the displacement field at the crack's location.

Strain maps, calculated from the displacement field, are an effective way to visualise the crack opening [57]; it creates an artificially high strain at its location, as shown in Figure 4c and d for HR and SR data respectively. This strain can be used to segment the crack quite effectively, as demonstrated in Figure 5. The figure shows the 3D crack within the specimen schematic, with tomography virtual slices in the *yz* plane, passing through the middle of the notch (see Figure 2b) and in the *xy* plane (z = 3.24 mm) to show the microstructure; the data are for the HR scan, loading sequence A (see Table 2). The strain field shown in Figure 5 is only for visualising the crack, without quantitative interpretation, since data are included from interrogation windows that overlap the crack opening and this affects the measurement. Hence no legend is provided, although qualitatively the darkest colours correspond to the highest crack opening and brighter colours correspond to lower openings.

To calculate the crack opening displacements (COD), the difference between the displacements (displacement along the y direction V_y) on either side the crack was used. Examples of the distribution of V_y along an arbitrary profile perpendicular to the nominal crack plane ($x = c_x$) (shown in Figure 4a and b) are plotted in Figure 6a

for HR and SR data, showing that the displacements either side of the crack are approximately constant (as observed previously in the less precise laboratory experiment [24]), i.e. there is no measureable strain in the material adjacent to crack. The average V_y on either side of the crack was calculated over the projected surface of the crack (see Figure 6b) using data only from image correlation windows that did not overlap the crack (for more detail on the method see [21]). An example of the obtained map of COD is shown in Figure 6c (SR scan at loading sequence A); the crack is observed to open more near its edge compared with the middle.

The COD profile along the crack from its mouth to its tip was obtained using the averaged values along a series of lines perpendicular to a sectioning plane that is defined in Figure 7a; Figure 7b shows an example of the reconstructed image on the sectioning plane at the middle of the chevron. The visible crack length in this slice is XX mm. Figure 7b shows two artefacts in the form of high contrast horizontal lines, which form along the edges of the notch. These artefacts are due to the strong difference in X-ray attenuation between air and graphite, and are generally observed at the boundaries of reconstructed images of specimens; here they arise from the edges of the notch. They do not interfere with the digital volume correlation analysis since they move with the deformation of the sample geometry.

The SR data for loading cycles A, C, F and G, which show a progressive development in the crack length, are shown in Figure 7c; measurements near the crack mouth are magnified in Figure 7d. The equivalent measurements obtained from HR data, which have less noise, are shown in Figure 7e for comparison (data were unfortunately not available from the crack tip). The average crack mouth opening displacement (CMOD) increased from 0.0298 to 0.0312 mm (SR scans - see Table 3 for full data, the values calculated from by analysis of SR and HR data at the same loading state differ by less than 5%). Using the RMS variation of the average *Vy* either side of the crack to obtain an approximate measurement error, the uncertainty in the SR data CMOD measurement is estimated at 0.0055 mm, which is significant compared to the average CMOD change with crack growth. However, comparison of loading sequence D and F, which were imaged at the same applied load, finds a difference of less than 0.001 mm in the average CMOD. The progressive increase in mean CMOD could therefore be due to crack extension or damage development.

To discern the effects of possible in-plane shear (mode II) and out-of-plane shear (mode III) loading that might have been applied to the specimen due to misalignment, crack displacements in the x and z directions were also calculated. Two volumes of 70×47×58 μm^3 (x×y×z) either side of the chevron were selected and their average displacements in x (V_x) and y (V_y) directions were extracted. The Mode II and mode III displacements were measured, with less an 0.5% variation, to be 0.0004 and 0.0016 mm, which are 1% and 5% of the mode I crack mouth opening displacement respectively. The components of mode II and mode III loading are thus negligible.

4 Finite element simulation

4.1 Linear elastic model

Three-dimensional linear elastic models with different crack lengths (a = 1.0 to 5.8 mm, at 0.2 mm steps) were created. Linear 8-node hexahedral elements (in total, 57984) were used to simulate the specimen; Figure 8a shows the overview of the finite element mesh. Nominal Gilsocarbon material properties [60] E = 10.9 GPa (elastic modulus) and ν = 0.2 (Poisson's ratio) were used. The steel wedge was modelled as a rigid body (its elastic modulus is more than ten times that of graphite) and frictionless contact between the rigid wedge and graphite specimen was defined; friction does not affect the relation between load and COD for this geometry [24]. Since the shape of the crack profile near the crack tip and the stress distributions around it were not the focus of this study, it was not necessary [61] to use specialised crack tip meshes such as the crack-type concentrated [62] and degenerated mesh [63] with singular elements [64].

A previous linear elastic finite element analysis has shown [24] that the gradient of the linear part of the COD profile from the crack mouth depends on the crack length. For each model, the normalised (COD/CMOD) crack openings in the xz plane were extracted from the finite element results. Each distribution, corresponding to a certain crack length, was then used to calculate the average normalised crack opening displacement, as was done for the experimental data. The normalised COD was then used to obtain the linear gradient from z = 0 and z = 3 mm, achieving correlation with R-values better than 0.98. A fifth order polynomial was fitted to the relation between the gradients and the model crack length (with R-value better than 0.99), from which

the crack lengths reported in Table 3 were interpolated using the experimentally measured gradients (see [24] for more details of the procedure). The crack length obtained was approximately 5.2 mm for all loading conditions (Table 3), which is about 1.6 mm longer than visually observed in the tomography absorption images (see section 2.2).

In the short rod chevron sample a stable propagating crack in an elastic material is in equilibrium with the fracture toughness for a/W<0.5 [42], consequently the crack lengths and the crack mouth opening displacements under load may be used with the linear elastic finite element analysis to estimate the fracture toughness. To this end, the mode I stress intensity factor K_I was calculated using Abaqus via the interaction integral method [65] for a crack length a = 5.2 mm (the average effective linear elastic crack length) and a crack mouth opening displacement of 0.0291. The stress intensity factor calculation by this method is largely independent of the mesh when dealing with mode I only [66], so there is no need for crack-type mesh. The measured crack mouth opening and effective linear elastic crack lengths for all tests are very similar (within 3%), so the linear FE-simulated stress intensity factor, K_I, was normalised by the modelled crack mouth opening displacement δ and crack length a, and this relationship was used to calculate the fracture toughness at each of the crack mouth opening displacements and crack lengths reported in Table 3.

$$\bar{K} = \frac{K_I}{\delta\sqrt{a}}$$

The values are reported in Table 3. The average fracture toughness (1.20 ± 0.18 MPa.mm$^{0.5}$) compares very well with the fracture toughness of Gilsocarbon graphite measured standard high constraint geometries (e.g. compact tension specimen [67]).

4.2 Cohesive zone model

The experimental data show the shape of the crack opening profile. The crack lengths obtained from its linear elastic analysis differ from the experimentally observed behaviour (see Figure 1a). To address this, a cohesive zone finite element simulation was carried out. Two half models (cut in the *xz* plane shown in Figure 6b) were created; the mesh on either side was identical. A tie equation was defined to attach

the two halves of the specimen remote from where fracture occurs: this was at the end of the chevron notch at z = 23 mm (i.e. where the threads were cut into the specimen, denoted by T in Figure 2a). From the tip of the chevron (i.e. the crack mouth at z=0) to z = 3.6 mm (observed in the experiment as the macroscopic crack tip) the two faces were not constrained and could open freely. A cohesive contact was defined from z = 3.6 mm to z = 23 mm. The model therefore allows the faces of the crack (from z = 0 to z = 3.6 mm) to open freely and for damage to occur from z = 3.6 mm to the end of the chevron. The sample is solid beyond the end of the chevron notch.

The elastic material properties were defined as in the linear elastic model, with a bilinear traction-separation law (see Figure 1b) applied to the cohesive contact area. It has been argued that the defining parameters for a bilinear traction law can be obtained experimentally [58]: the cohesive energy G_f may be assumed to be equivalent to the critical energy release rate in a highly constrained geometry (e.g. compact tension test) and the critical stress σ_c may be assumed to be equivalent to the ultimate stress in a tensile test. For Gilsocarbon graphite, the typical uniaxial flexural strength has been measured to be 28 MPa [21] and the critical energy release rate to be 260 J/m^2 [22].

An example of the simulation of a deformed specimen (when CMOD = 0.0291 mm, i.e. loading sequence A) is shown in Figure 8b and c. The distribution of damage in the xz plane coincident with the crack is shown in Figure 8d. There is full separation (damage parameter = 1) in front of the 3.6 mm separated crack over a distance of 1.6 mm, giving a total crack length of 5.2 mm. This is in excellent agreement (within 1%) with the effective crack length obtained from the linear elastic model using the measured COD profile (see Table 3). The comparison between the experimentally measured COD distribution (HR and SR) and linear elastic and cohesive contact models is shown in Figure 8e.

To study the sensitivity of the simulation to the cohesive parameters, the effects of changing G_f and σ_c over reasonable experimental ranges were examined (~±30% variation). In the first set of simulations the cohesive energy remained constant (G_f = 260 J/m^2) and the critical stress was varied from 23 to 35 MPa; each simulation was loaded until the crack mouth opening displacement reached the experimentally measured value for loading sequence A (i.e. 0.0291 mm). The second series used a

constant critical stress (σ_c = 28 MPa) and varied the cohesive energy G_f from 180 to 340 J/m^2. Profiles of the scalar damage variable (d) (d = 0 before damage initiation, d=1 when fully softened corresponding to local failure of the interface) at the middle of the chevron are shown in Figure 9a and b. The effects on the average COD/CMOD profiles are shown in Figure 9c and d, compared with the linear elastic model for crack lengths a = 3.6 mm and a = 5.2 mm.

The crack opening profiles of experimental data, pure elastic model (with crack length a = 5.2 mm) and cohesive zone model with G_f = 260 J/m^2 and σ_c = 28 MPa are compared in Figure 10a and b for the SR and HR data respectively, using the 3D data to examine the opening at the middle and edge of the chevron (see Figure 6c for the definition of chevron edge and chevron middle). The data are normalised by the measured crack mouth opening displacement (δ = 0.0291 mm). The cohesive zone model predicts greater opening in the damaged zone at the edge, compared to the middle, and this is also seen in the experimental data.

5 Discussion

Combined digital volume correlation (DVC) and X-ray computed tomography (XCT) was used in this study to measure the full-field 3D displacements in a short bar chevron notch specimen fabricated from Gilsocarbon graphite. The artificial high strains arising from the crack opening displacements were exploited to segment the crack, which was otherwise difficult to achieve in the absorption contrast images of this porous and complicated microstructure. The three-dimensional interaction of the propagating crack with the microstructure could be observed by combining the strain visualisation and the XCT data; the propagating crack passes around a filler particle, for instance (see Figure 5), indicating that these are resistant to fracture. Such crack behaviour cannot be readily observed in two-dimensional studies. More importantly, the measured displacement field can be used to quantify the crack opening displacement (e.g. Figure 6c). The three-dimensional data show that the crack tip region is more open around the edges than at its middle. The average profile of crack opening displacement (Figure 7) confirms that the response of graphite is far from linear elastic and close to the characteristics of the strip yield or cohesive zone model that is commonly applied to concrete (a quasi-brittle material).

Linear elastic modelling was employed to estimate the effective crack length from the gradient of the measured crack opening profile, obtaining crack lengths that were approximately 1.5 mm longer than the macroscopic cracks observed in the absorption contrast tomographic images. Cohesive contact modelling, using a simple bilinear traction-separation law with experimentally measureable parameters (cohesive energy and critical stress), correctly predicted both the general characteristics of the measured crack opening profile and the same effective crack length as that obtained using a simple elastic model, fitted to the crack mouth opening profile. This is consistent with the effects of a significant fracture process zone, softened by damage to behave in a mechanically similar manner to a longer effective crack [68].

These unique observations show that a cohesive zone forms in front of the crack that cannot be modelled using linear elastic assumptions. The HR data show that the fully unloaded (sequence C) CMOD measurement reduces only by 7%, i.e. the crack does not close fully. This may be due to the wedge not being removed from the specimen; the previous laboratory study [24] showed significant relaxation of the crack opening when the wedge was fully removed. That study found a residual opening of the unloaded crack, which was attributed either to wedging by surface roughness, or permanent inelastic deformation in the fracture process zone. Loading sequence H was carried out to remove the wake of the macroscopic crack (a = 3.6 mm – see Figure 7b) and any wedging contribution. The data show that if there is a residual opening ahead of the crack tip from inelastic deformation, it is below the measurement resolution and is insignificant.

The sensitivity study of the bilinear traction-separation law in the cohesive zone model (Figure 9) shows that the cohesive energy and critical stress have a combined effect on the distribution of the damage index; this arises from the interaction between damage and the stress field in the sample and the fracture process zone is therefore not independent of the sample geometry. The main effect of the critical stress is on the extent of the fully damaged area whereas the cohesive energy mainly changes the gradient of the damage distribution. This is also apparent in the opening displacement profiles within the fracture process zone. Better simulation of the fracture process zone would require a more complete description of traction-separation than the bilinear relationship, although the latter is clearly a fair approximation.

Comparison of the measured and modelled profiles at the middle and edge of the crack (Figure 10q and b) show that there is a good agreement (better than 10%) between the cohesive zone model and the experiment over the length of the macroscopic crack. There is also no significant difference over this region between the opening at the middle and edge. However, within the fracture process zone (i.e. from z = 3.6 to z = 5.2 mm), the difference between the model and experiment increases. In the middle the model under predicts the COD, whilst it over predicts significantly at the edge near the free surfaces.

The middle and edge of the fracture process zone experience different degrees of constraint from the surrounding material. The through thickness variation of constraint (plane stress and plane strain in extreme conditions) is usually referred to as out-of-plane constraint. Using the behaviour shown in Figure 9, if it were assumed that the critical stress was independent of constraint level, the cohesive energy should be decreased to fit better the experimental results for the middle; but to fit the edge measurements the cohesive energy should be increased. Similar effects are found if the cohesive energy is assumed to be constraint independent. It is not possible to use a single pair of cohesive energy and critical stress parameters to simulate the observed crack openings in the fracture process zone. This dependency on out-of-plane constraint is in agreement with the expectation that the quasi-brittle behaviour of materials with a degree of inelastic behaviour, such as graphite, will be similar that observed in elastic-plastic materials; these exhibit a prominent constraint effect (see for example [69]). This effect may become significant in some sample geometries (such as notch specimens with a/W<0.5 under flexure [40]), and is in agreement, for instance, with the observed dependency of the fracture resistance curve in polygranular graphite on the stress state [21].

Cohesive zone modelling can be applied in two forms: cohesive contact and brittle cracking [55]. The cohesive contact technique used in this study is computationally less expensive than brittle cracking, but requires a predefined crack propagation direction and assumes a smeared 2D fracture process zone in front of the crack tip. The cohesive contact method is suitable for controlled crack propagation in a test specimen such as here, and from the point of view of engineering design it is always preferred for cracks with known propagation paths. The alternative brittle cracking

technique does not require a pre-determined path and could be used to simulate the same macromechanical behaviour, including the development of a diffuse 3D fracture process zone. The experimental techniques applied here are now being developed to observe and measure the fracture process zone and its properties in more detail, aiming to quantify the effects of constraint on the traction-separation law and its dependence on microstructure. This may be used to understand better the relative behaviour of small test specimens and larger components, for instance, and to support more advanced predictive modelling of fracture resistance and crack paths in complex stress states.

6 Conclusions

- X-ray computed tomography and digital volume correlation were used to measure the 3D full-field displacements in polygranular Gilsocarbon graphite during quasi-static fracture.
- The three-dimensional crack opening displacements were mapped, identifying a damaged fracture process zone with a size of approximately 1.5 mm. This is consistent with the expected quasi-brittle fracture behaviour of this material.
- Three-dimensional cohesive zone modelling was used to simulate successfully the experimentally observed crack opening and fracture process zone.
- An effect of out-of-plane constraint on the fracture resistance is deduced. This is proposed to be a general characteristic of quasi-brittle materials. Hence a more accurate model would require a cohesive law with constraint dependent parameters.

Acknowledgements

This work was carried out with the support of the Diamond Light Source and the authors acknowledge the beamtime award at the Joint Engineering, Environmental and Processing (I12 – JEEP) beamline (Experiment EE7119). Dr M. Drakopoulos and Dr C. Reinhard from I12 are gratefully acknowledged for their technical support. Mr X. Mengyin, Mr D. James and Ms A. Fargette are thanked for helping with carrying out the experiment. MM and TJM gratefully acknowledge the support of Oxford Martin School and MM acknowledges the support of Linacre College, Oxford through a Junior Research Fellowship. The Manchester X-Ray Imaging Facility

(Professor P.M. Mummery, in particular) is gratefully acknowledged for loan of the loading rig. Finally, EDF Energy is thanked for providing us with the material.

References

[1] Mostafavi M, Marrow TJ. Fatigue and Fracture of Engineering Materials and Structures 2012;35:695.

[2] Nakhodchi S, Smith DJ, Flewitt PEJ. J. Mater. Sci. 2012;In press.

[3] Becker TH, Tait RB. Fracture and slow crack characteristics of nuclear grade graphite using the double torsion beam technique. 12th International Conference on Fracture. Ottawa, Canada, 2009.

[4] Droillard C, Lamon J. J. Am. Ceram. Soc. 1996;79:849.

[5] Hambli R. Med. Biol. Eng. Comput. 2013;51:219.

[6] Berto F, Lazzarin P, Ayatollahi MR. Carbon 2012;50:1942.

[7] Berto F, Lazzarin P, Marangon C. Mater. Des. 2012;41:421.

[8] Hillerborg A, Modeer M, Petersson PE. Cem. Concr. Res. 1976;6:773.

[9] Rosa AL, Yu RC, Ruiz G, Saucedo L, Sousa JLAO. Eng. Fract. Mech. 2012;82:195.

[10] Song SH, Paulino GH, Buttlar W. Eng. Fract. Mech. 2006;73:2829.

[11] Ho FH. Graphite design handbook. San Diego, CA: General Atomics, 1988.

[12] Ayatollahi MR, Torabi AR. Carbon 2010;48:2255.

[13] Karihaloo BL. Fracture Mechanics and Structural Concrete. New York: Longman Scientific and Technical Publishers, 1995.

[14] Frantík P, Veselý V, Keršner Z. Adv. Eng. Softw. 2013;In Press.

[15] Ouagne P, Neighbour GB, McEnaney B. JORUNAL OF PHYSICS D: APPLIED PHYSICS 2002;35:927.

[16] Mostafavi M, Smith DJ, Pavier MJ. Fatigue Fract. Eng. Mater. Struct. 2010;33:724.

[17] Guo W. Eng. Fract. Mech. 1993;46:93.

[18] Guo W. Eng. Fract. Mech. 1993;46:105.

[19] Guo W. Eng. Fract. Mech. 1995;51:51.

[20] Tvergaard V, Hutchinson JW. J. Mech. Phys. Solids 1992;40:1377.

[21] Mostafavi M, McDonald SA, Çetinel H, Mummery PM, Marrow TJ. Carbon 2013;59:325.

[22] Becker TH, Marrow TJ, Tait RB. J. Nucl. Mater. 2011;414:32.

[23] Hodgkins AD, Marrow TJ, Mummery PM, Marsden BJ, Fok ASL. J. Mater. Sci. Technol. 2006;22:1045.

[24] Mostafavi M, McDonald SA, Mummery PM, Marrow TJ. Eng. Fract. Mech. 2013;http://dx.doi.org/10.1016/j.engfracmech.2012.11.023.

[25] Barenblatt GI. The mathematical theory of equillibrium cracks in brittle fracture. In: Dryden HL, von Kármán T, Kuerti G, van den Dungen FH, Howarth L, editors. Advances in Applied Mechanics (Volume 7). New York: Academic Press, 1962.

[26] Dugdale DS. J. Mech. Phys. Solids 1960;8:100.

[27] Tarleton E, Charalambides MN, Leoppard C. Comput. Mater. Sci. 2012;64:183.

[28] Ingraffea AR, Saouma V. Numericak modelling of discrete crack propagation in reinforced concrete and plain concrete. In: Shi G, Di Tomasso A, editors. Fracture Mechanics of Cocnrete. Dordrecht: Martinus Nihhoff Publishers, 1985. p.171.

[29] Ruiz G, Ortiz M, Pandolfi A. Int. J. Numer. Methods Eng. 2000;48:963.

[30] Yu RC, Ruiz G. Int. J. Fract. 2006;141:357.

[31] Karihaloo BL, Abdalla HM, Xiao QZ. Cem. Concr. Res. 2006;36:171.

[32] Choupani N. Eng. Fract. Mech. 2008;75:4363.

[33] Harper PW, Hallet SR. 75 2008.

[34] Chandra N, Li H, Shet C, Ghonem H. Int. J. Solids Struct. 2002;39:2827.

[35] Siegmund T, Brocks W. Int. J. Fract. 1999;99:97.

[36] Yang QD, Cox BN, NAlla RK, Ritchie RO. Biomaterials 2006;27:2095.

[37] Zou Z, Fok ASL, Marsden BJ, Oyadiji SO. Eng. Fract. Mech. 2006;73:318.

[38] Jones AN, Hall GN, Joyce MR, Hodgkin AD, Wen K, Marrow TJ, Marsden BJ. J. Mater. Sci. 2008;381:152.

[39] Tsang DKL, Marsden BJ. J. Nucl. Mater. 2006;350:208.

[40] R6. Assessment of the Integrity of Structures Containing Defects: British Energy, 2001.

[41] Brocks W, Scheider I. Numerical aspects of the path-dependence of the *J*-integral in incremental plasticity - How to calculate reliable *J*-values in FE analyses. Köln-Porz: Institute für Werkstofforschung, 2001.

[42] Ouchterlony F. Int. J. Rock. Mech. Mining. Sci. 1988;25:71.

[43] DaVis. User's Manual. Gottingen: LaVision GmbH,, 2012.

[44] Sutton MA, McNeill SR, Helm JD, Chao YJ. Top. App. Phys. 2000;77:323.

[45] Keane RD, Adrian RJ. Appl. Scu. Res. 1992;49:191.

[46] Becker TH, Mostafavi M, Tait RB, Marrow TJ. Fatigue Fract. Eng. Mater. Struct. 2012;35:971.

[47] Cook A, Duff J, Stevens N, Lyon S, Sherry AH, Marrow TJ. ECS Trans. 2010;25:119.

[48] Duff J, Marrow TJ. CORROSION SCIENCE 2012;68:34.

[49] Rahimi S, Engelberg DL, Duff J, Marrow TJ. J. Microsc. 2009;233:423.

[50] Roux S, Rethore J, Hild F. J. Phys. D: App. Phys. 2009;42:1.

[51] Yusof F, Withers PJ. J. Strain Anal. Eng. Des. 2009;44:149.

[52] Bay BK, Smith TS, Fyhire DP, Saad M. Exp. Mech. 1999;39:217.

[53] Franck C, Hong S, Maskarinec SA, Tirrell DA, Ravichandran G. Exp. Mech. 2007;47:427.

[54] Smith TS, Bay BK, Rashid MM. Exp. Mech. 2004;42:272.

[55] ABAQUS. User's Manual: Dassault Systèmes Simulia Corp., Providence, Rhode Island, Version 6.10, 2010.

[56] Camanho PP, Dávila CG, De Mora MF. J. Compos Mater. 2003;37:1415.

[57] Mostafavi M, Marrow TJ. Eng. Fract. Mech. 2011;78:1756.

[58] Cornec A, Scheider I, Schwalbe KH. Eng. Fract. Mech. 2003;70:1963.

[59] Munch B, Trtik P, Marone F, Stampanoni M. Optics Expr. 2009;17:8567.

[60] Joyce MR, Marrow TJ, Mummery PM, Marsden BJ. Eng. Fract. Mech. 2008;75:3633.

[61] Henshell RD, Shaw KG. Int. J. Numer. Methods Eng. 1975;9:495.

[62] Tracey DM. Nucl. Eng. Des. 1974;26:282.

[63] Wilson WK. Some crack tip finite elements for plane elasticity. In: Corten HT, Gallagher JP, editors. Stress Analysis and Growth of Cracks: Preceedings of the 1971

National Symposium on Fracture Mechanics: Part I. Philadelphia: ASTM STP 513, 1971.

[64] Barsoum RS. Int. J. Numer. Methods Eng. 1976;10:25.

[65] Stern M, Becker EB, Dunhma RS. Int. J. Fract. 1976;12:359.

[66] Sinclair GB. Int. J. Fract. 1985;28:3.

[67] Hodgkins AD, Marrow TJ, Wootton MR, Moskovic R, Flewitt PEJ. Mater. Sci. Technol. 2010;26:899.

[68] Bažant ZP. Fracture and Size Effect: In concrete and other quasibrittle materials: CRC Press INC, 1998.

[69] Kim J, Gao G, Srivatsan TS. Int. J. Solids Struct. 2003;40:7357.

Tables

Table 1 –Dimensions

Parameter	Symbol	Measure	Unit
Notch thickness	t_o	1	mm
Specimen diameter	D	24	mm
Notch height	Z_o	12	mm
Notch angle	θ	55	Degree (°)
Specimen length	L	35	mm
Wedge angle	ϕ	10	Degree (°)
Ligament	W	23	mm

Table 2 – Loading sequence

Loading sequence	Resolution*	Load (N)	Description
0	HR, SR	0	As-received
A	HR, SR	310	Cycle 1 -loaded
B	HR	250	Cycle 1 – Partially unloaded
C	HR, SR	0	Cycle 1 - unloaded
D	SR	330	Cycle 2 – loaded
E	SR	280	Cycle 2 – load drop
F	SR	330	Cycle 2 – repeat
G	SR	340	Cycle 3
H	SR	0	Cut specimen

* SR – standard resolution (5μm voxel size); HR – high resolution (1.8μm voxel size)

Table 3 – Crack characteristics

Loading sequence		Observed crack length *	Estimated linear elastic crack length †	Crack mouth opening displacement (CMOD) ‡	Crack opening compliance (CMOD/F)	Estimated fracture toughness §
		mm	mm	mm	10^{-6} × mm/N	MPa.$m^{0.5}$
A	SR	3.40 ± 0.02	5.14 ± 0.01	0.0291 ± 0.0048	93.87 ± 15.48	1.19 ± 0.19
	HR	3.45 ± 0.01	5.25 ± 0.02	0.0315 ± 0.0011	101.61 ± 3.55	1.21 ± 0.04
B	SR	-	-	-	-	-
	HR	3.31 ± 0.00	5.21 ± 0.02	0.0311 ± 0.0011	124.40 ± 4.40	NA
C	SR	3.40 ± 0.05	5.12 ± 0.01	0.0283 ± 0.0050	NA	NA
	HR	3.41 ± 0.02	5.15 ± 0.04	0.0294 ± 0.0017	NA	NA
D	SR	3.43 ± 0.01	5.29 ± 0.01	0.0283 ± 0.0049	85.76 ± 14.85	1.17 ± 0.20
	HR	-	-	-	-	-
E	SR	3.43 ± 0.02	5.19 ± 0.01	0.0291 ± 0.0049	103.93 ± 17.5	1.17 ± 0.20
	HR	-	-	-	-	-
F	SR	3.60 ± 0.02	5.08 ± 0.01	0.0295 ± 0.0051	89.39 ± 15.45	1.19 ± 0.21
	HR	-	-	-	-	-
G	SR	3.68 ± 0.02	5.16 ± 0.00	0.0312 ± 0.0055	91.76 ± 16.18	1.24 ± 0.22
	HR	-	-	-	-	-

* the error is the visual variation in the crack lengths
† the error is calculated from the variation in the normalised crack opening gradients
‡ the error is calculated from the variation of the average displacement
§ the error is calculated from the variation in the crack length and normalised opening gradients

Figures

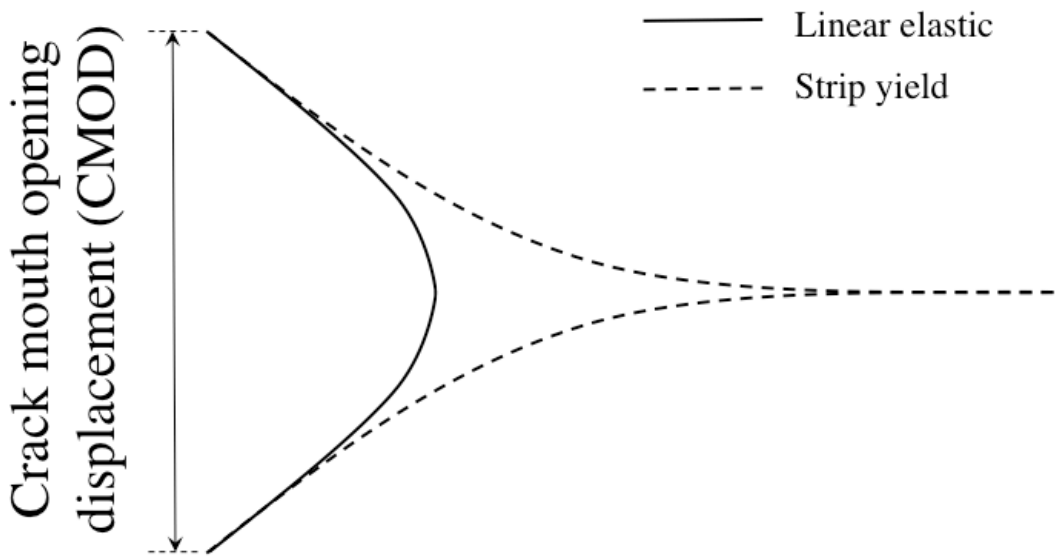

(a)

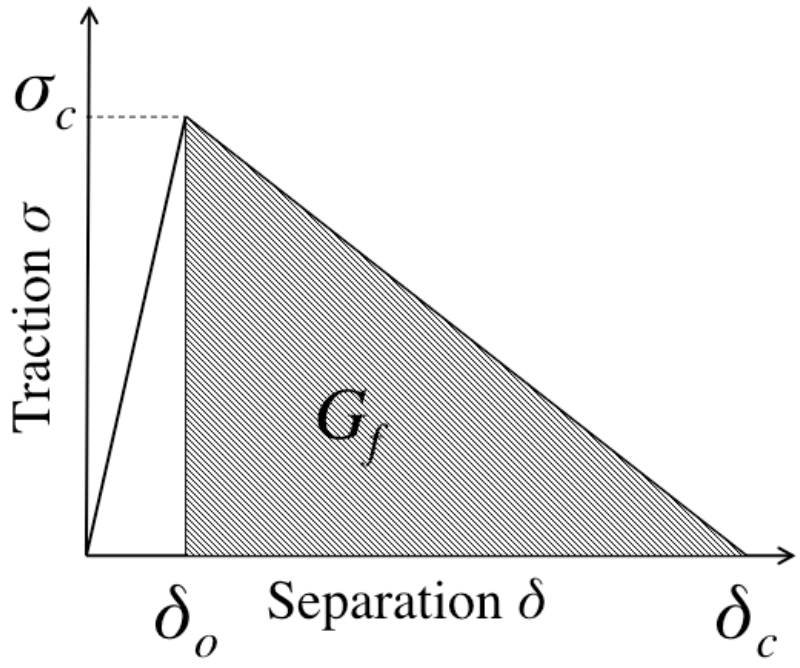

(b)

Figure 1 – Cohesive zone model (a) crack opening profile (b) traction-separation law

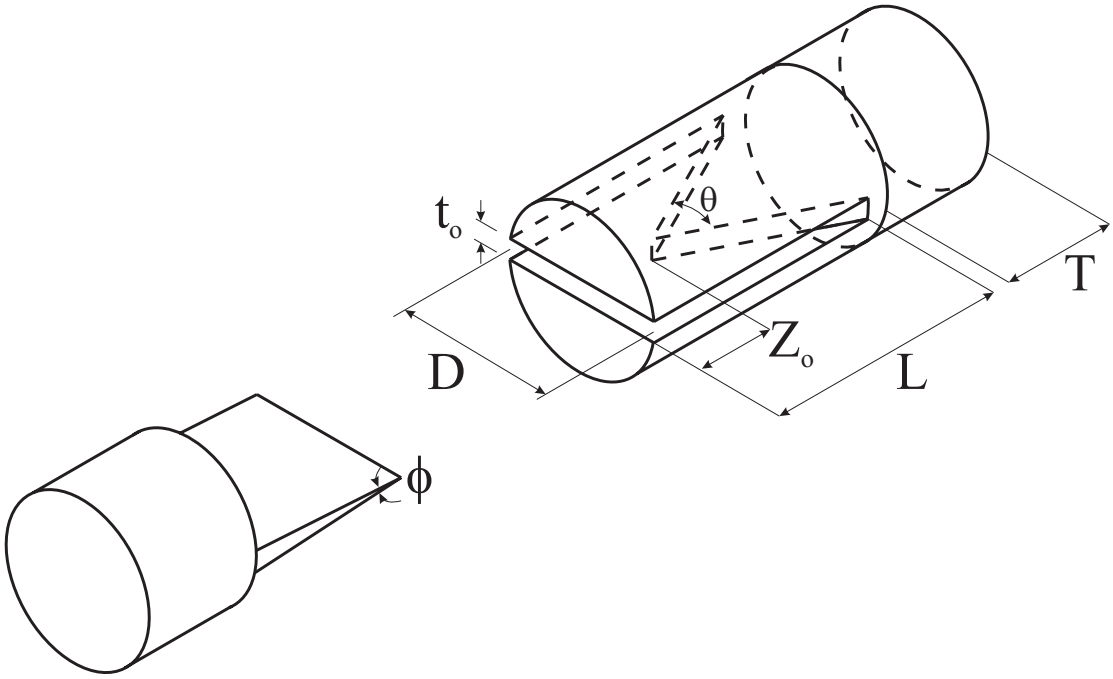

(a)

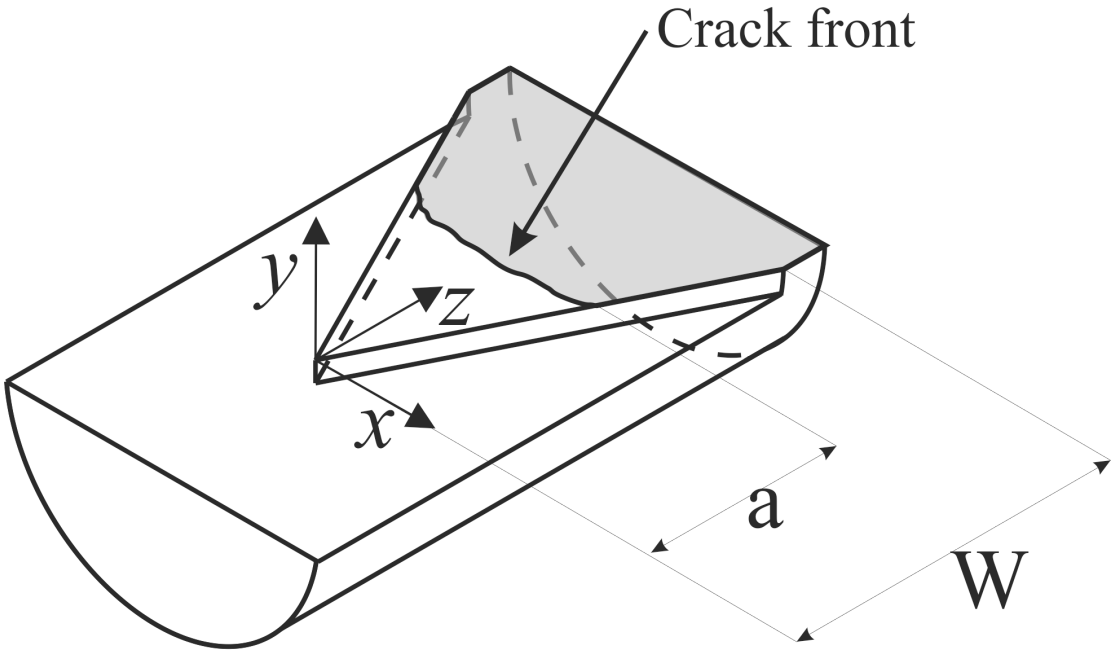

(b)

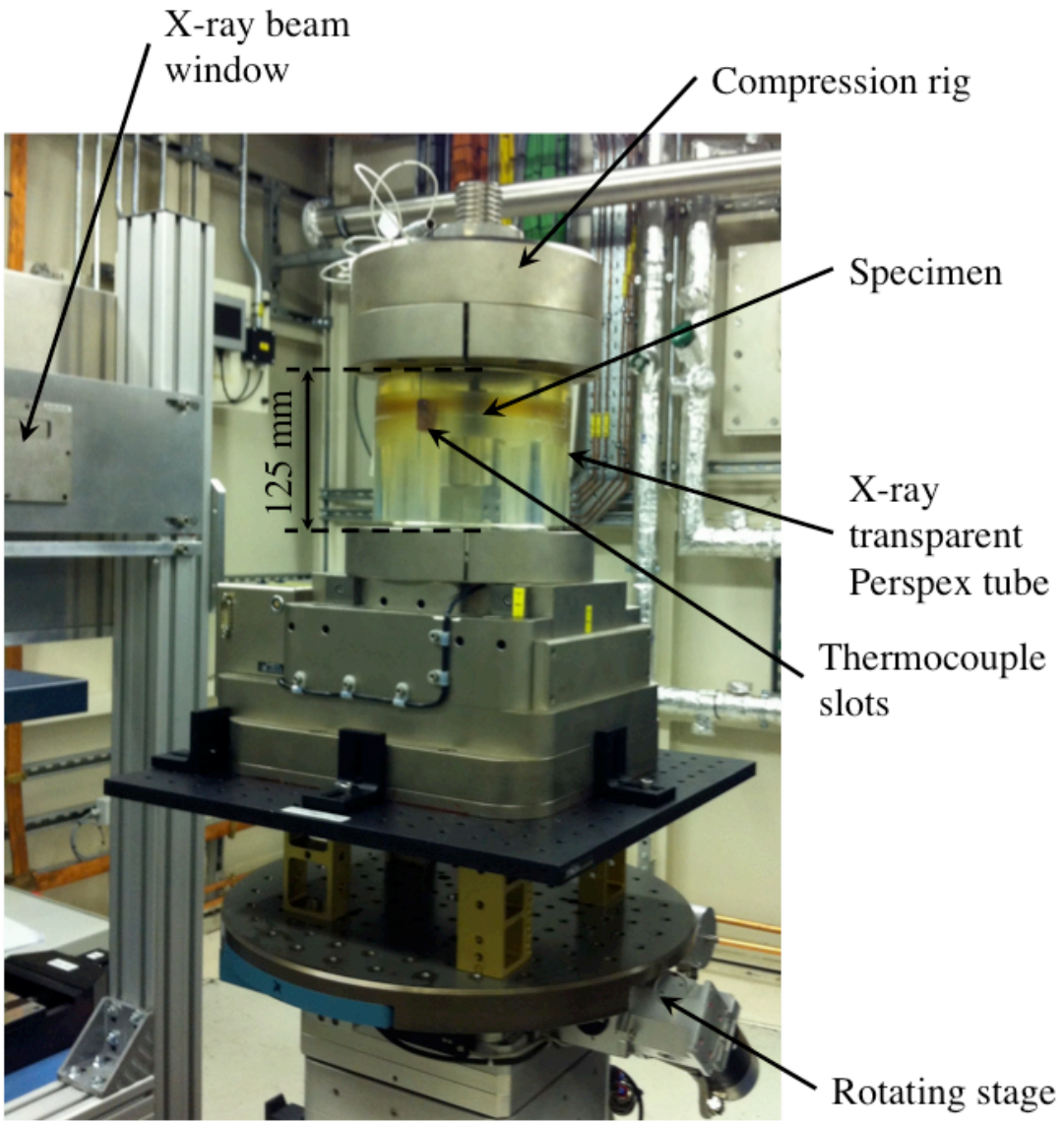

(c)

Figure 2 – Experiment overview (a) Chevron notch specimen (b) half chevron notch specimen (c) experiment setup in the beamline

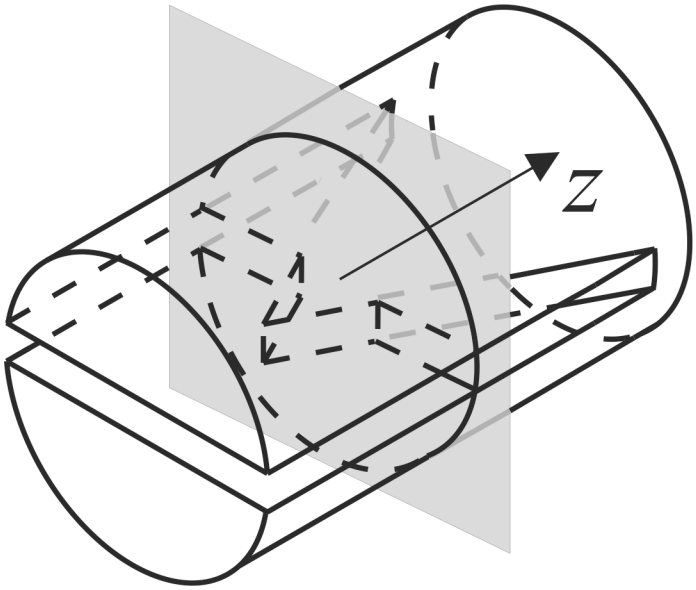

(a)

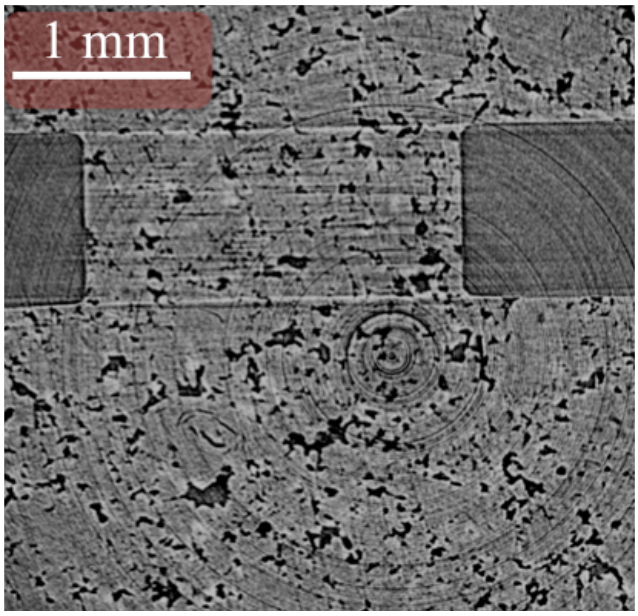

(b)

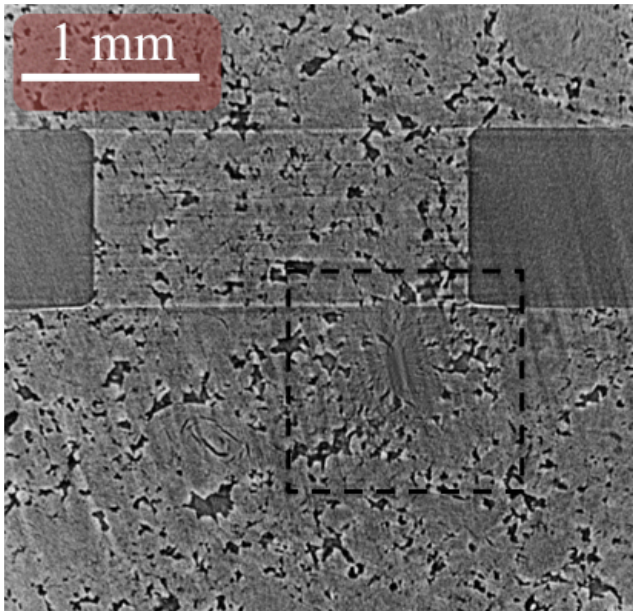

(c)

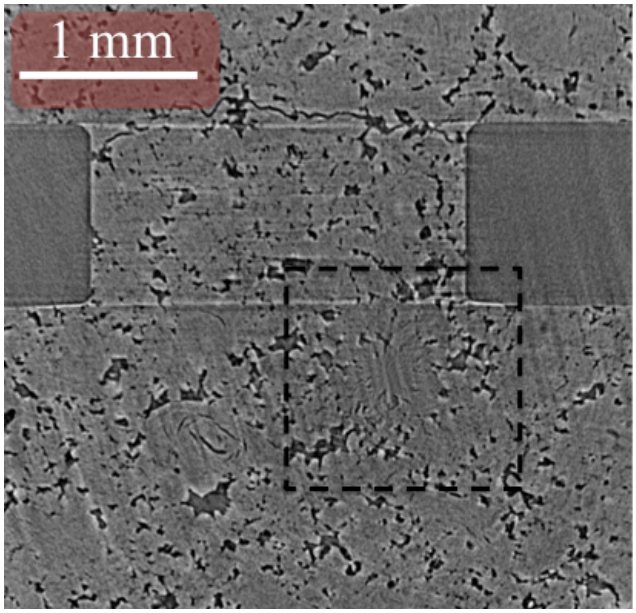

(d)

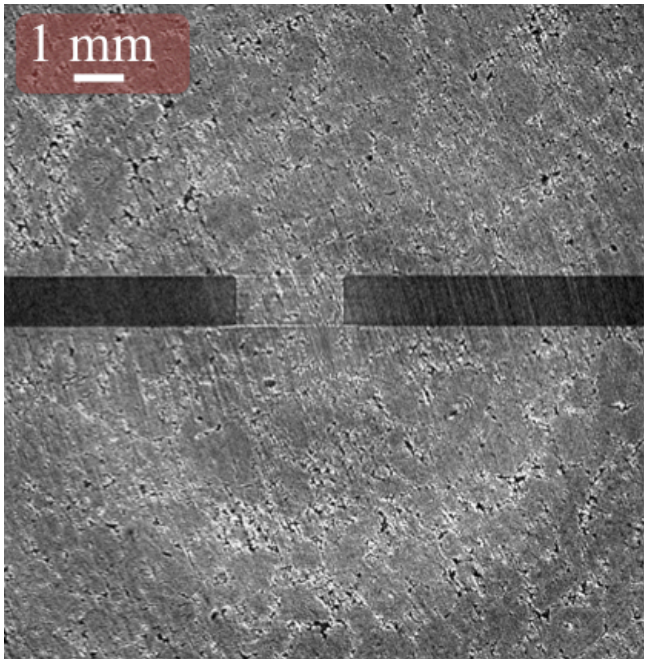

(e)

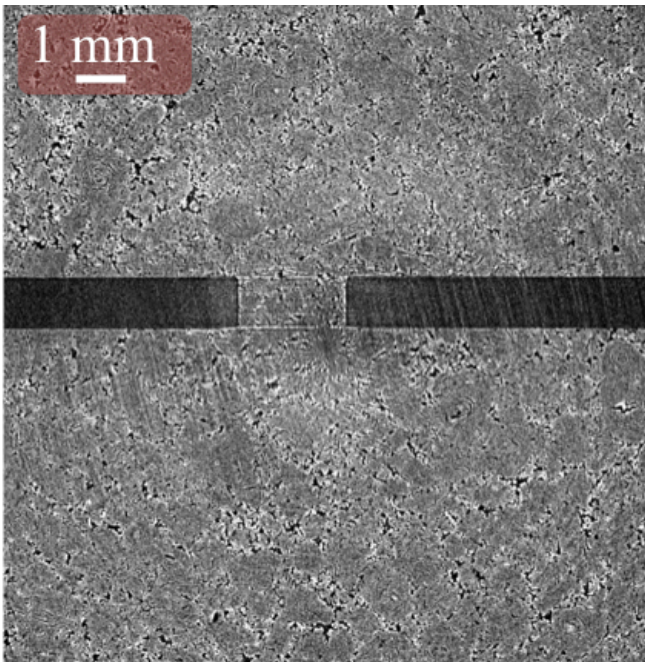

(f)

Figure 3 – Example of reconstructed virtual slice (a) virtual slice orientation (b) HR uncracked slice example without ring artefact correction (c) HR (cropped field of view 2672×2672 pixels) – uncracked (d) HR cracked (cropped field of view identical to c) (e) SR (cropped field of view 3122×3122 pixels) – uncracked (f) SR (cropped field of view identical to e)– cracked - The dashed box shows the artefact produced by combined wavelet-Fourier ring artefact removal algorithm.

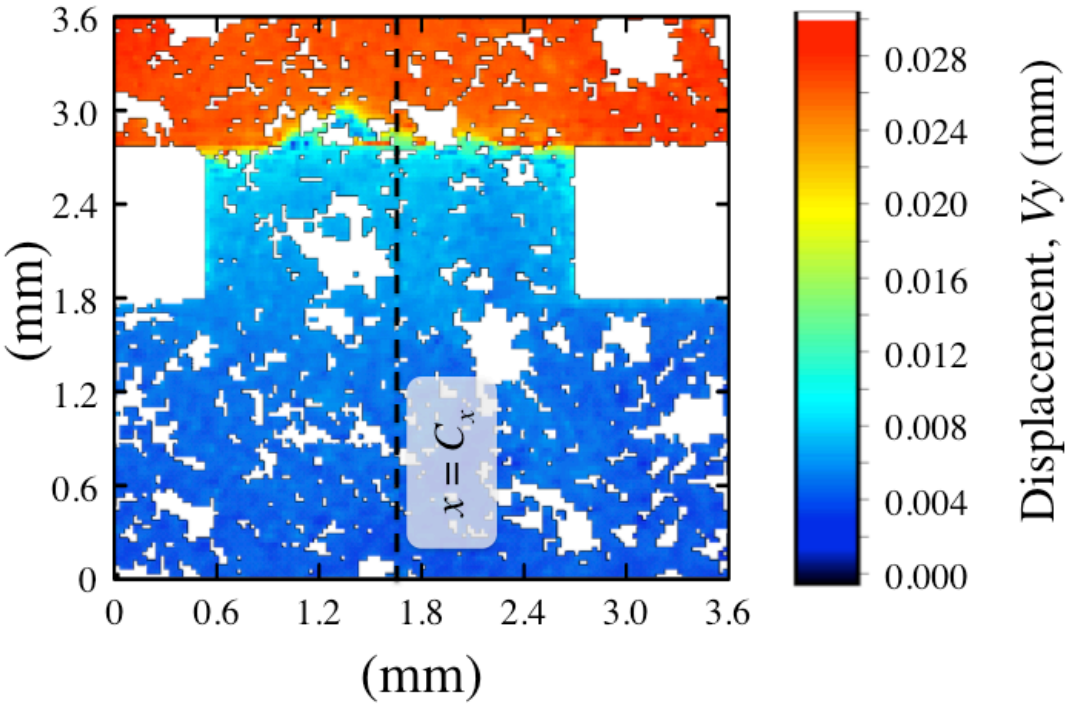
3.6
3.0
2.4
1.8
1.2
0.6
0
(mm)
0
0.6
1.2
1.8
2.4
3.0
3.6
(mm)
$x = C_x$
0.028
0.024
0.020
0.016
0.012
0.008
0.004
0.000
Displacement, Vy (mm)

(a)

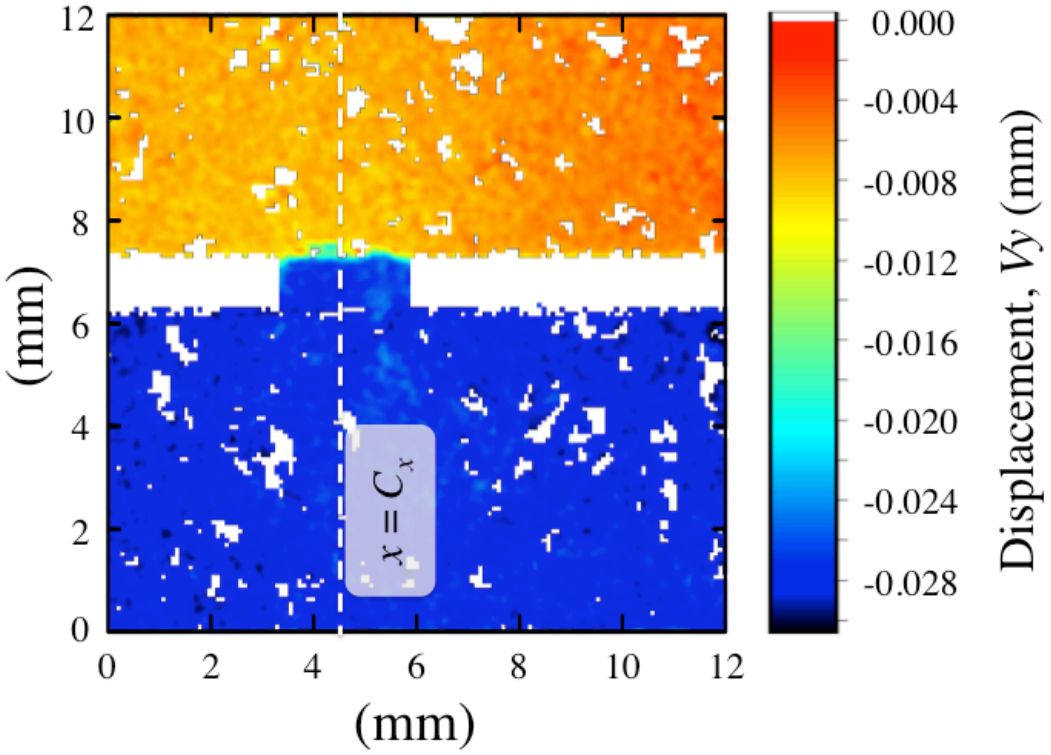
12
10
8
6
4
2
0
(mm)
0
2
4
6
8
10
12
(mm)
$x = C_x$
0.000
-0.004
-0.008
-0.012
-0.016
-0.020
-0.024
-0.028
Displacement, Vy (mm)

(b)

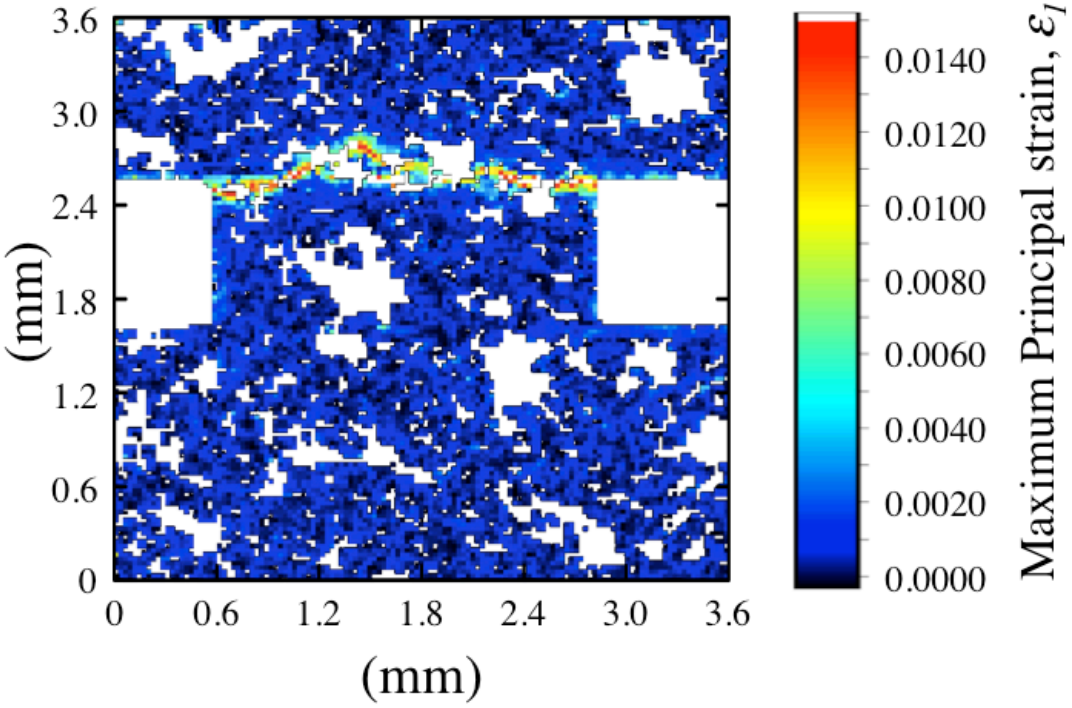

(c)

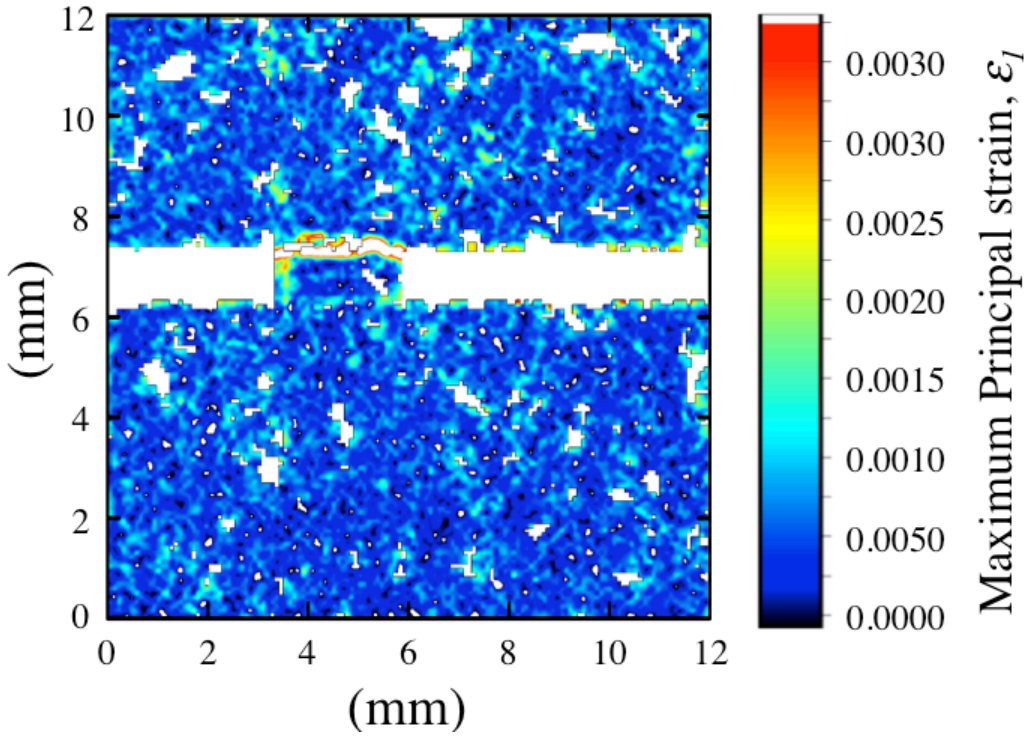

(d)

Figure 4 – Examples of opening displacement and maximum principal strain distribution of the virtual slice shown in figure 2 (a) HR opening displacement (U_y) (b) SR opening displacement (U_y) (c) HR maximum principal strain (ε_1) (d) SR maximum principal strain (ε_1)

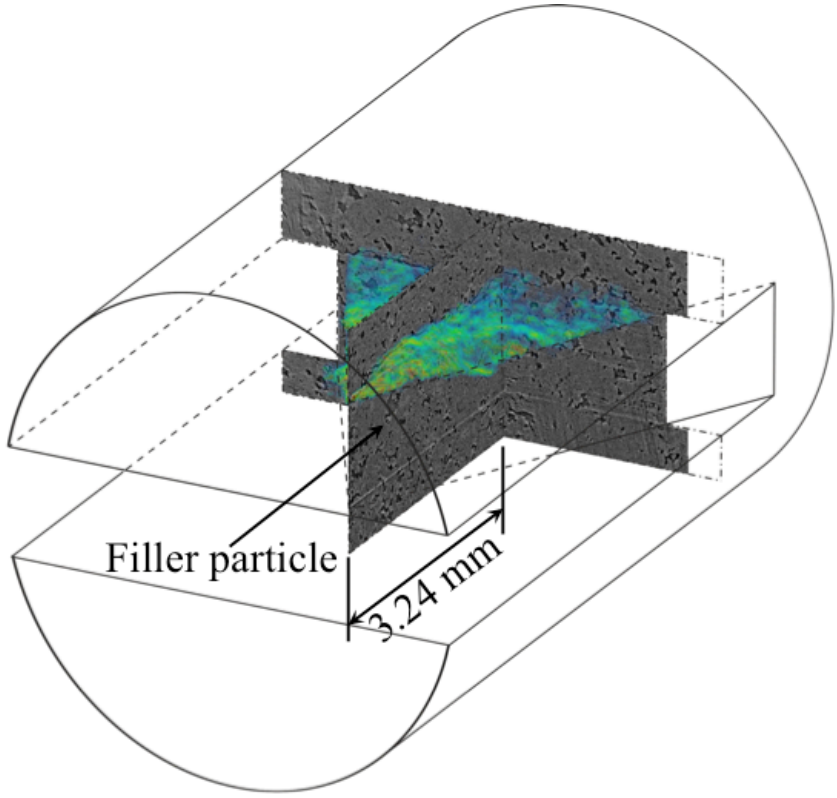

Figure 5 – Three-dimensional representation of the microstructure (HR) and maximum principal strain

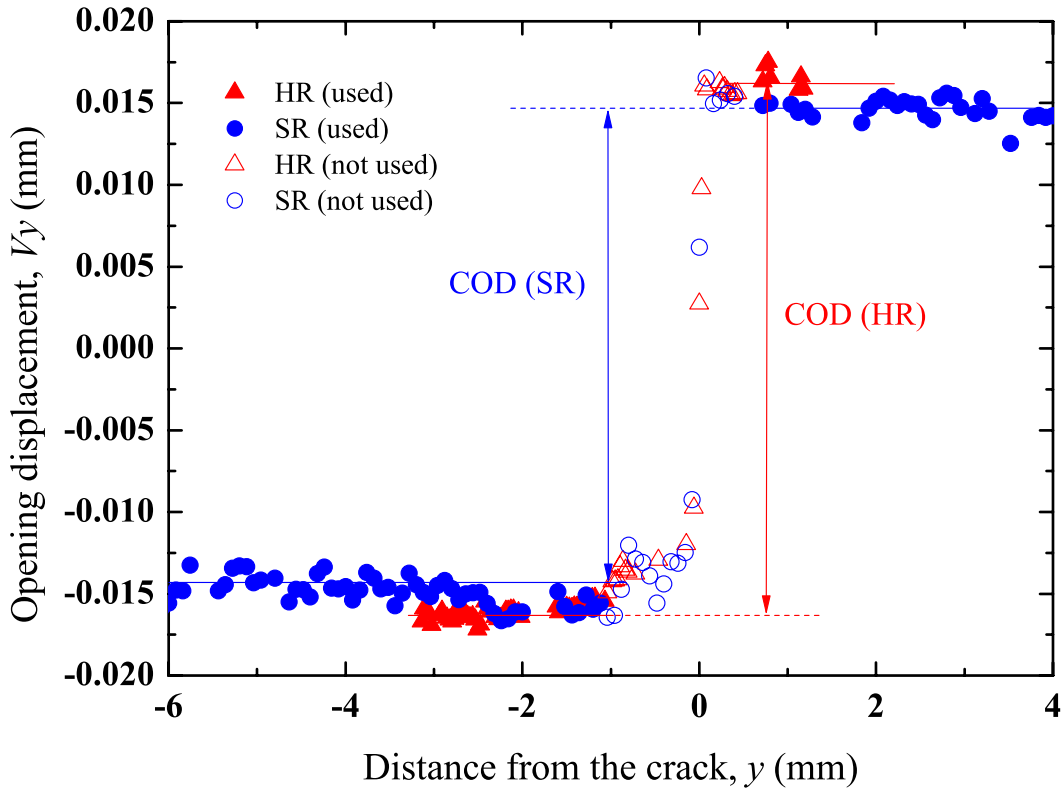
0.020
0.015
0.010
0.005
0.000
-0.005
-0.010
-0.015
-0.020
-6
-4
-2
0
2
4
Opening displacement, Vy (mm)
Distance from the crack, y (mm)
HR (used)
SR (used)
HR (not used)
SR (not used)
COD (SR)
COD (HR)

(a)

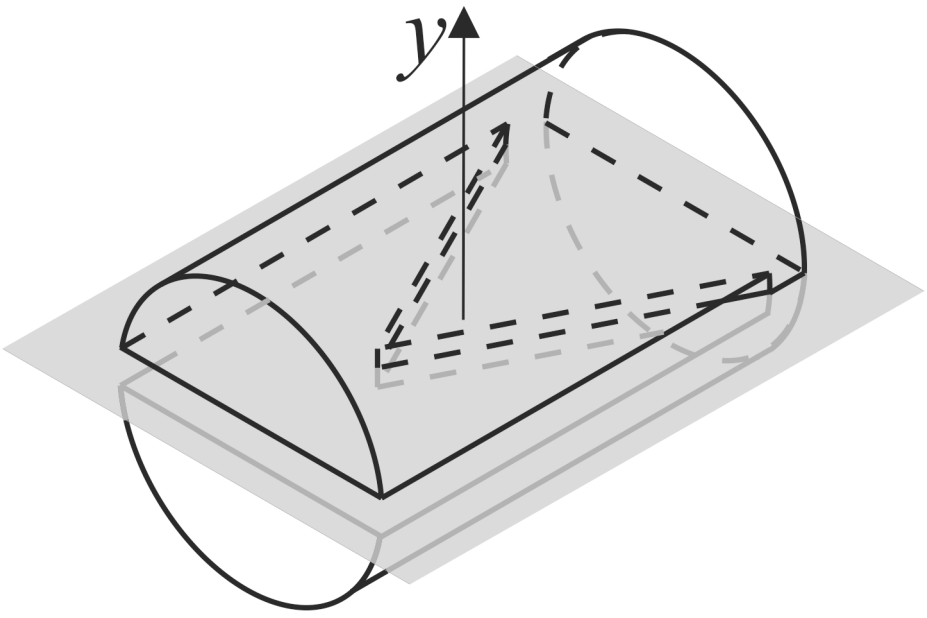
y

(b)

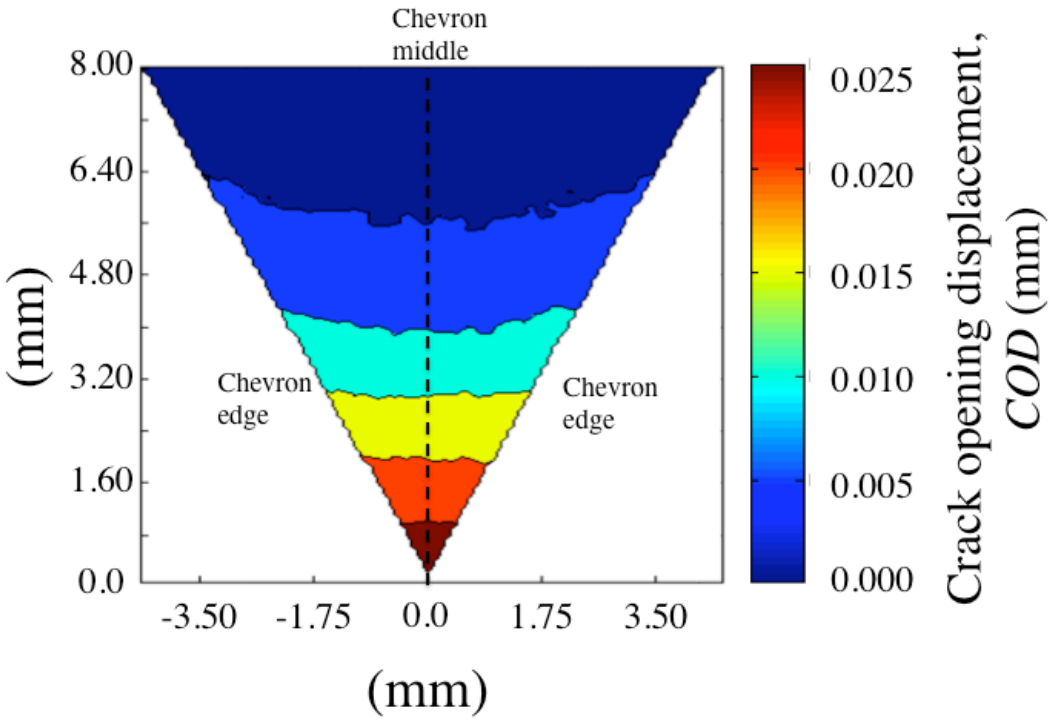

(c)

Figure 6 – measured crack opening displacement (COD) (a) example of the opening displacement profile perpendicular to the crack along $x = c_x$ (see Figs. 4a and b) – solid line shows the length on which the average has been calculated (b) virtual slice (c) COD distribution on the virtual slice at the first loading cycle (A) calculated from the SR data

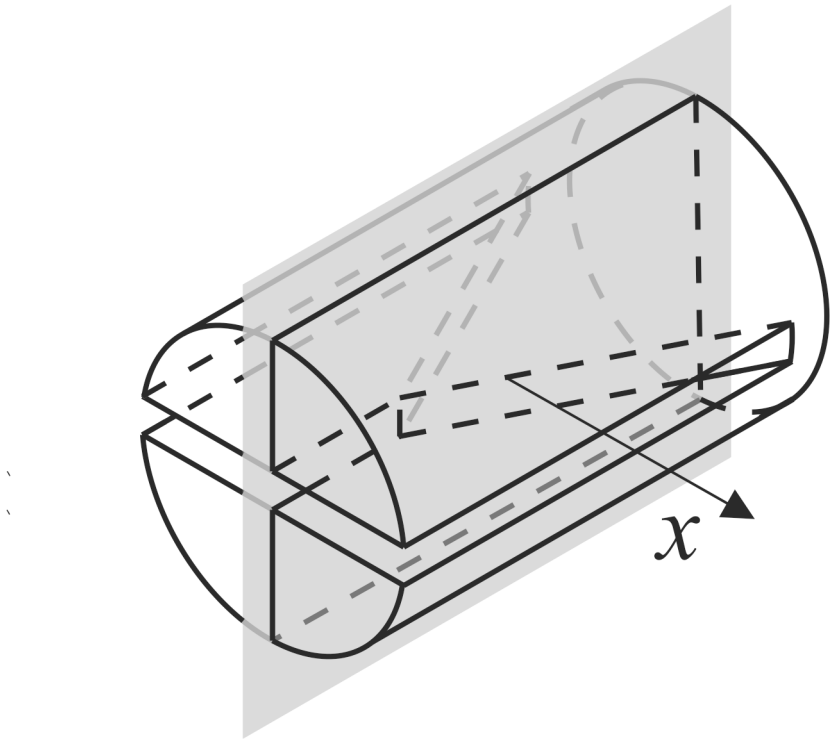

(a)

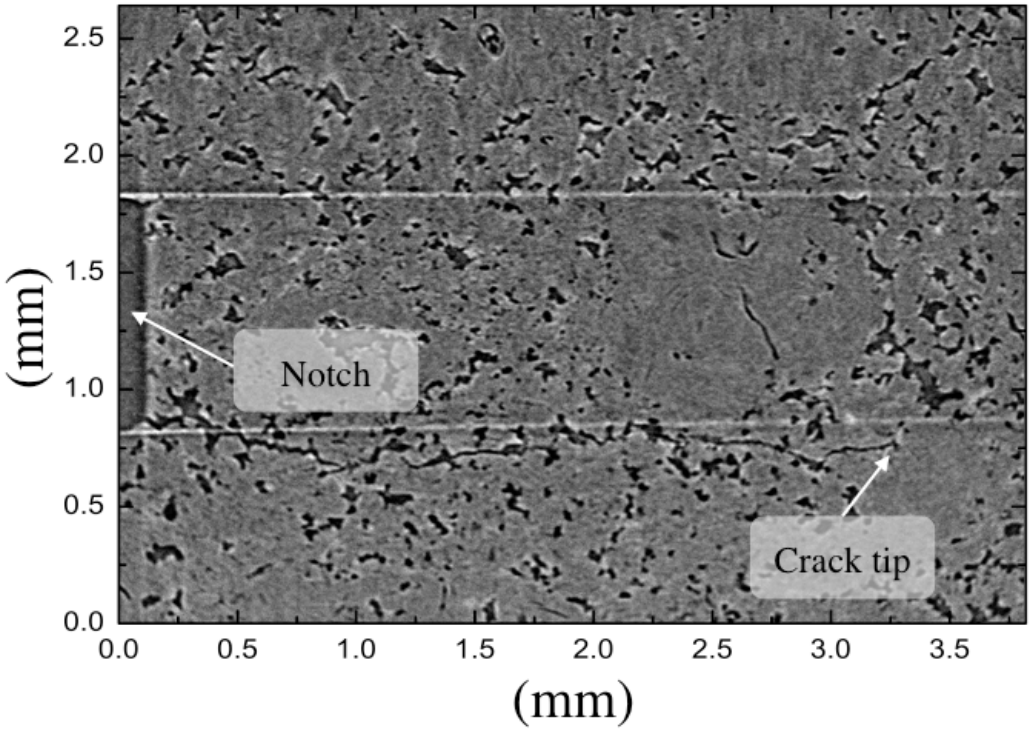

(b)

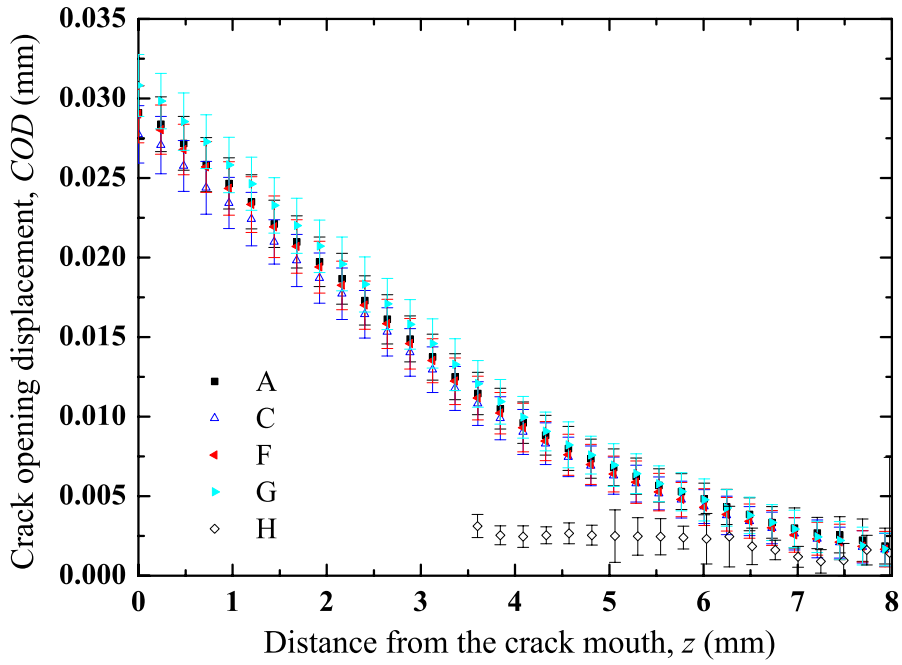
Crack opening displacement, COD (mm)
0.035
0.030
0.025
0.020
0.015
0.010
0.005
0.000
A
C
F
G
H
0
1
2
3
4
5
6
7
8
Distance from the crack mouth, z (mm)

(c)

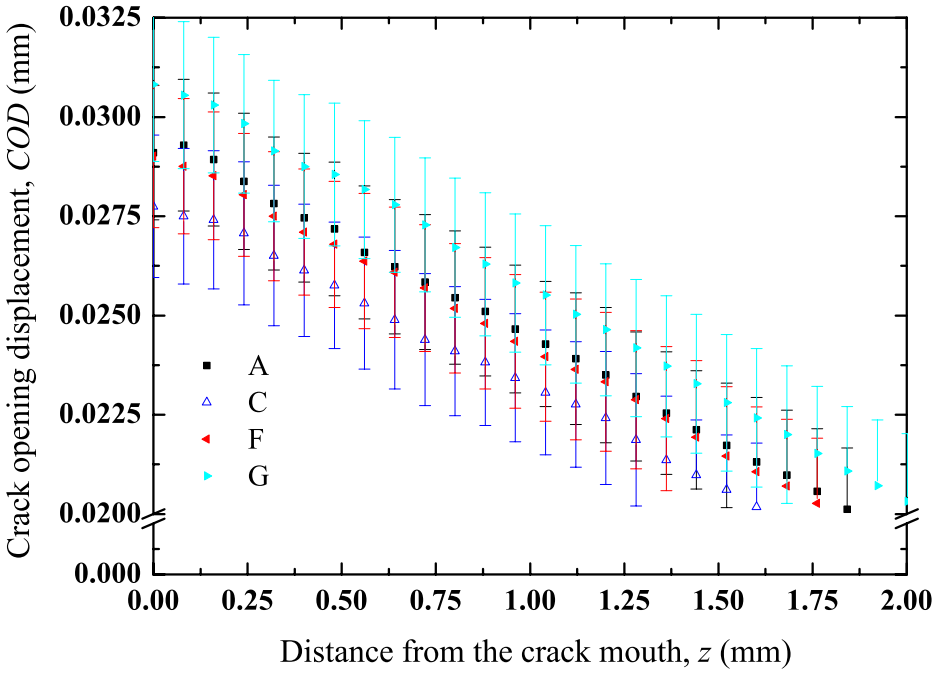
Crack opening displacement, COD (mm)
0.0325
0.0300
0.0275
0.0250
0.0225
0.0200
0.000
A
C
F
G
0.00
0.25
0.50
0.75
1.00
1.25
1.50
1.75
2.00
Distance from the crack mouth, z (mm)

(d)

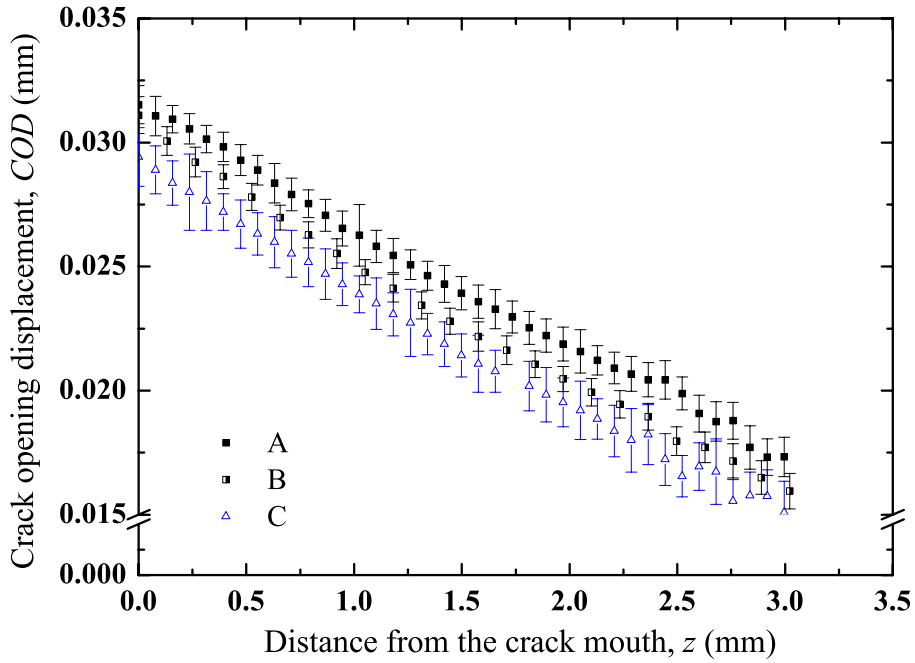

(e)

Figure 7 – Crack opening profiles: (a) virtual slice on whch the profile is shown; (b) example of reconstructed virtual slice loading sequence A (c) averaged COD distribution at different loading cycles (SR data); (d) focus on the crack mouth opening displacement (SR data); (e) averaged COD distribution at different loading cycle (HR data - only every fifth data point is shown)

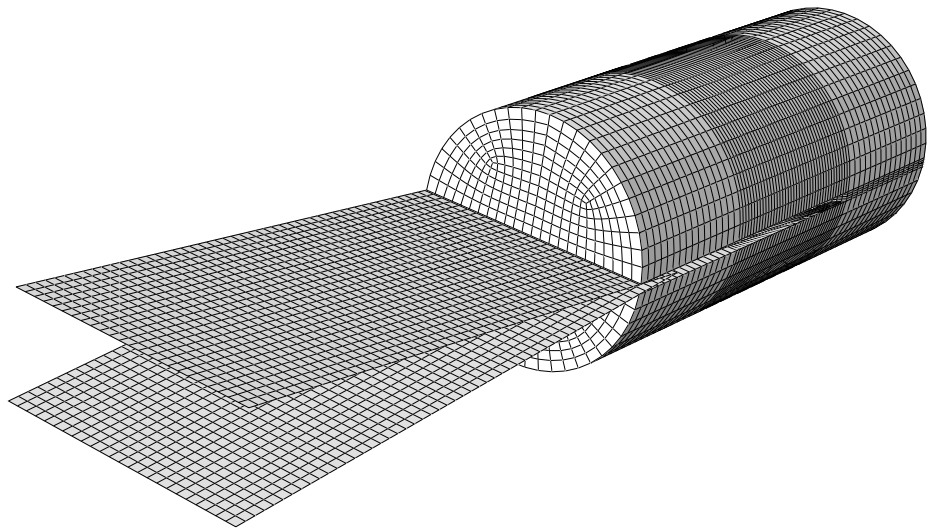

(a)

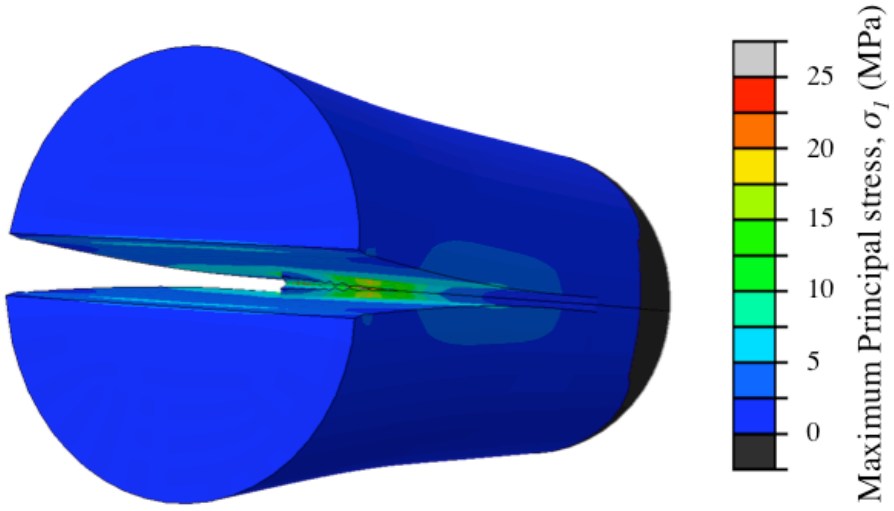
25
20
15
10
5
0
Maximum Principal stress, σ_1 (MPa)

(b)

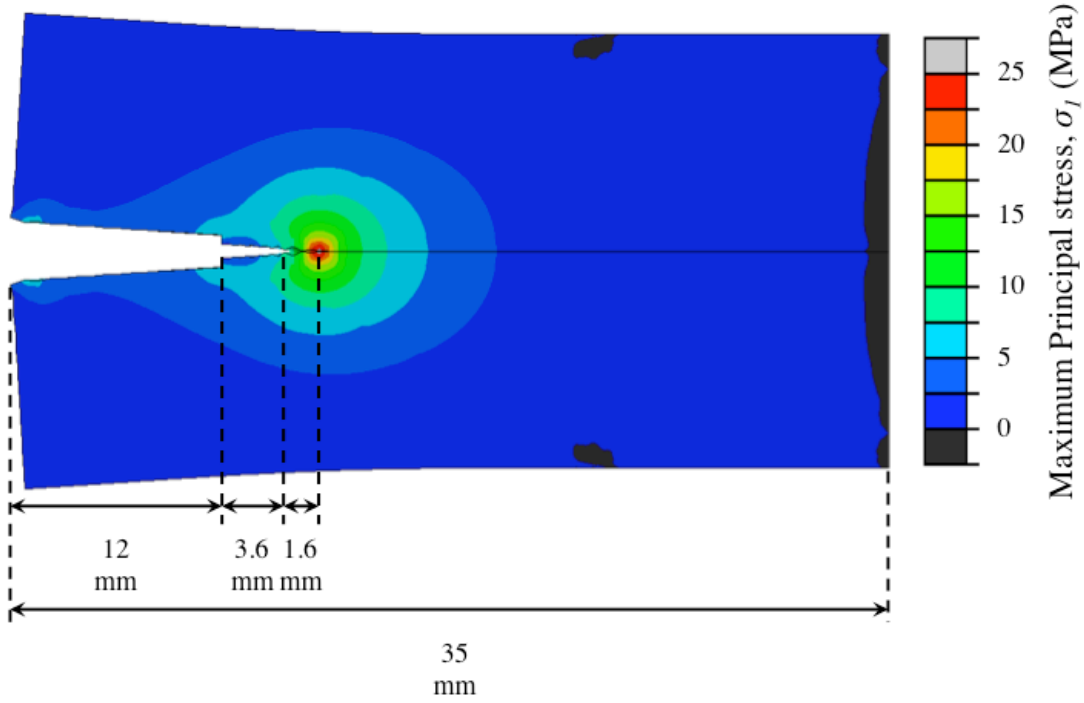
25
20
15
10
5
0
Maximum Principal stress, σ_1 (MPa)
12 mm
3.6 mm
1.6 mm
35 mm

(c)

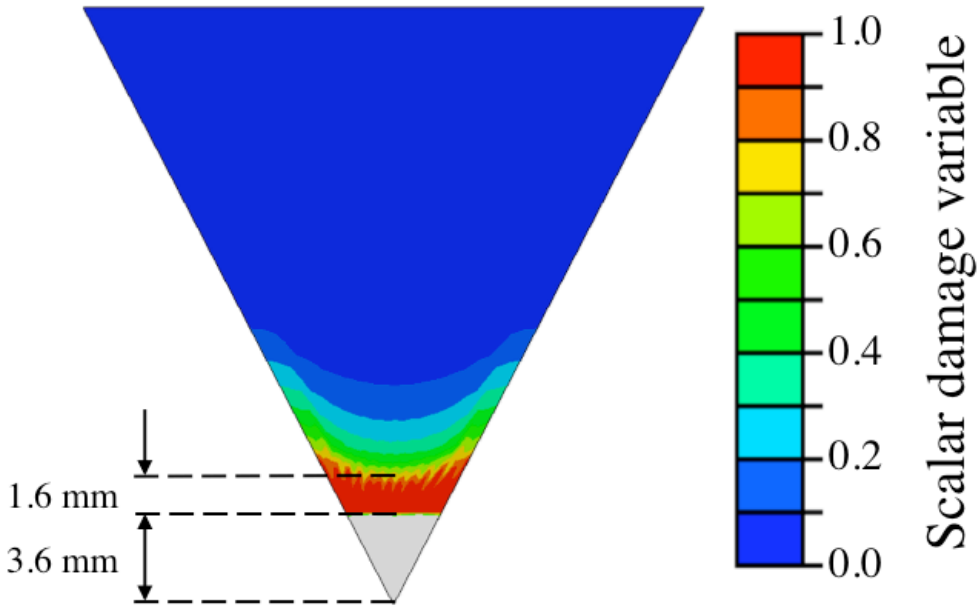

(d)

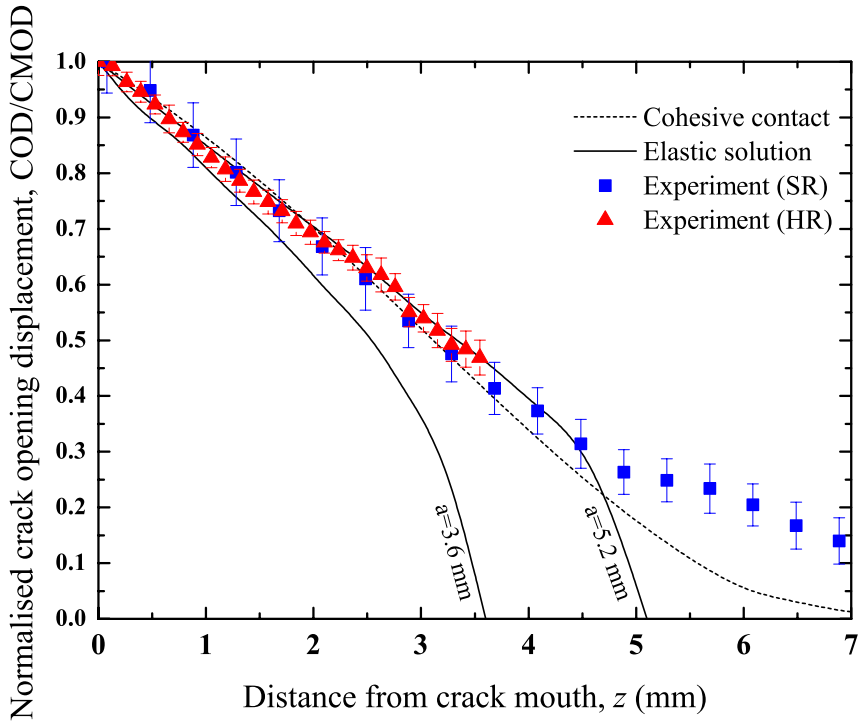

(e)

Figure 8 – Finite element simulation and experiment comparison: (a) FE mesh; (b) example of full deformation; (c) example of deformation in *yz* plane; (d) damage distribution in *xz* plane; (e) experimentally measured COD in comparison with elastic and cohesive contact finite element models. The deformations in (b) and (c) are magnified 25 times.

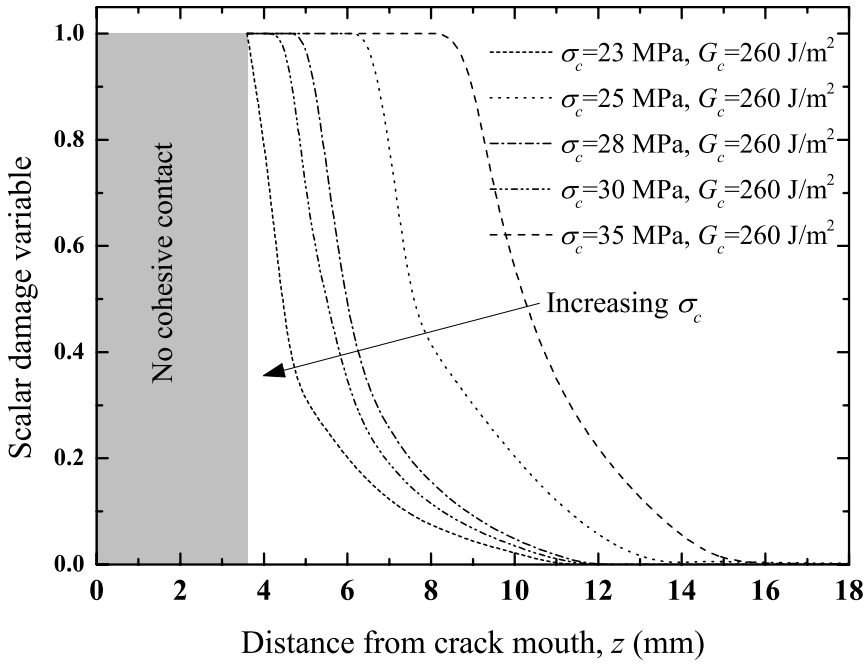
Scalar damage variable
Distance from crack mouth, z (mm)
No cohesive contact
σc=23 MPa, Gc=260 J/m2
σc=25 MPa, Gc=260 J/m2
σc=28 MPa, Gc=260 J/m2
σc=30 MPa, Gc=260 J/m2
σc=35 MPa, Gc=260 J/m2
Increasing σc

(a)

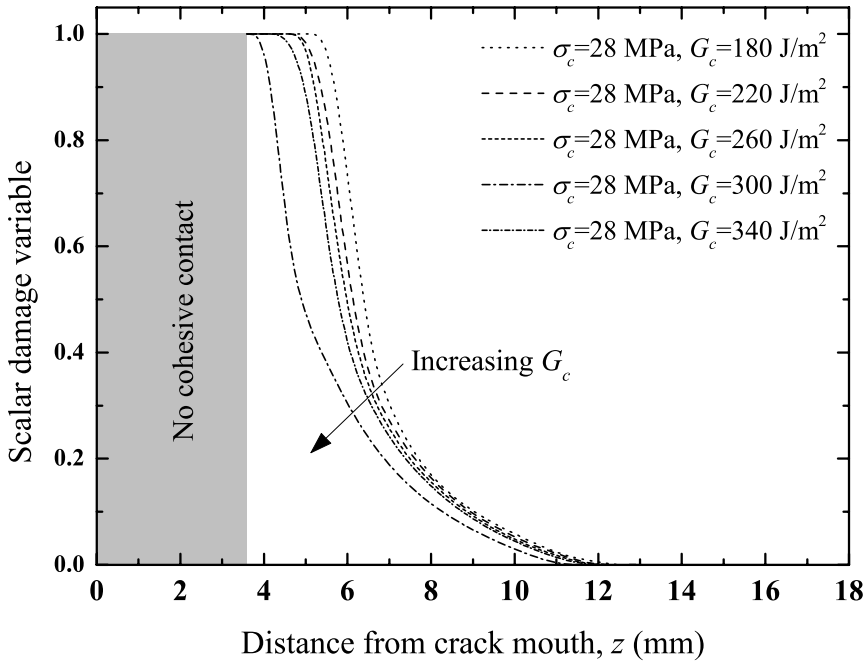
Scalar damage variable
Distance from crack mouth, z (mm)
No cohesive contact
σc=28 MPa, Gc=180 J/m2
σc=28 MPa, Gc=220 J/m2
σc=28 MPa, Gc=260 J/m2
σc=28 MPa, Gc=300 J/m2
σc=28 MPa, Gc=340 J/m2
Increasing Gc

(b)

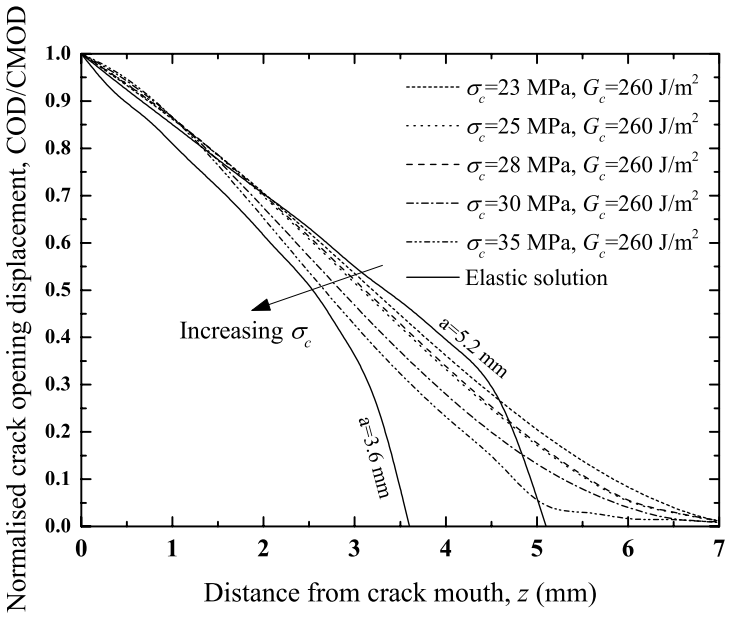

(c)

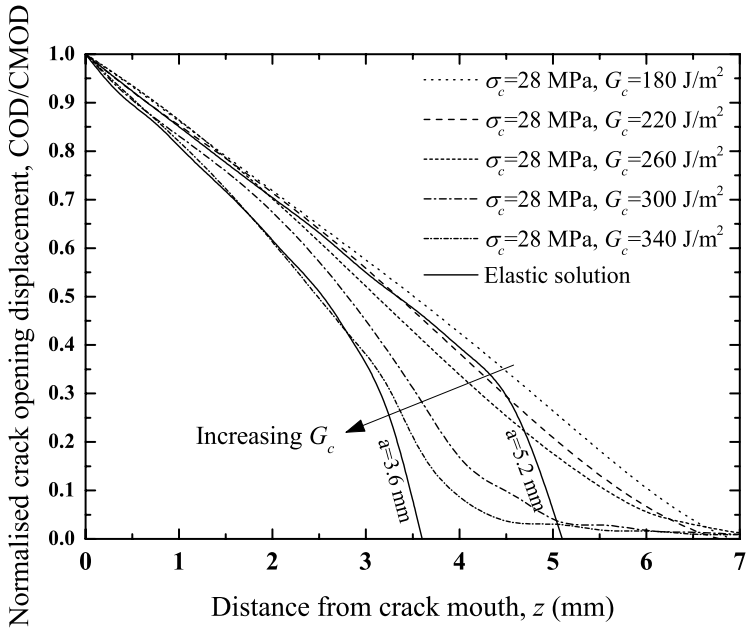

(d)

Figure 9 – Sensitivity study of the bilinear traction-separation law: (a) damage profile with respect to varying critical stress; (b) damage profile with respect to varying cohesive energy; (c) crack opening profile with respect to varying critical stress; (d) crack opening profile with respect to varying cohesive energy

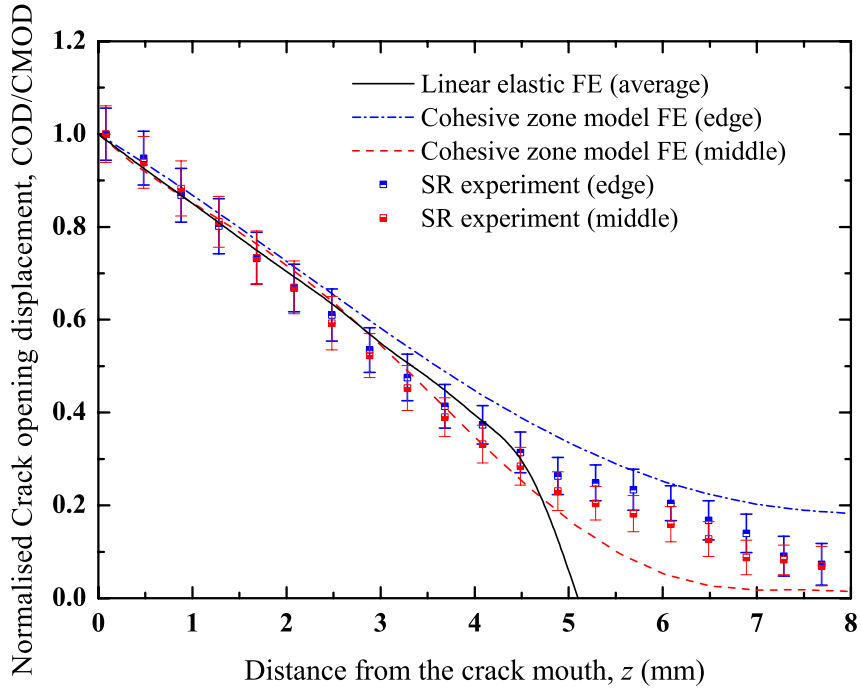

(a)

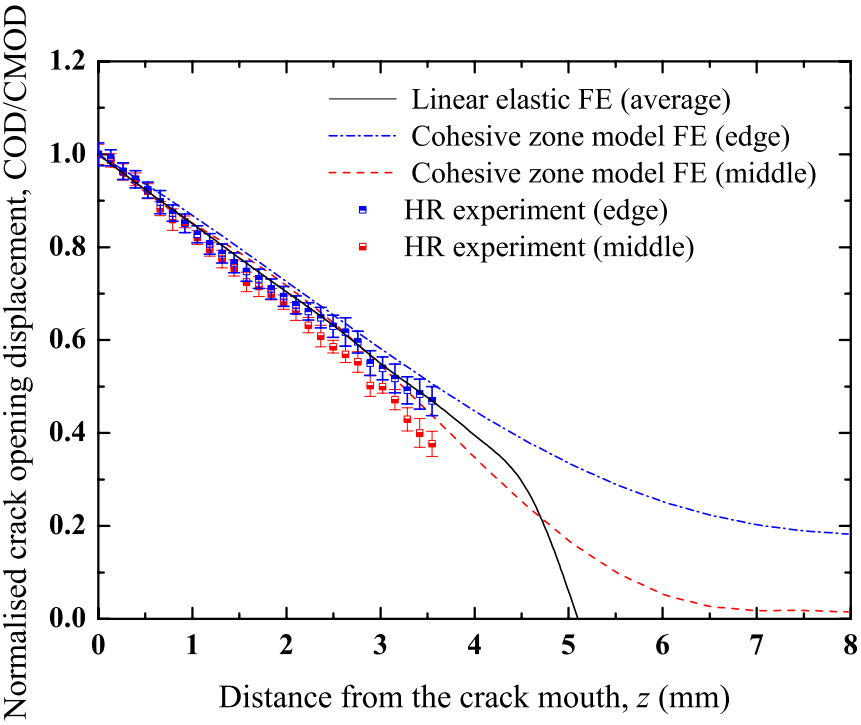

(b)

Figure 10 – Finite element simulation and experimental measurement comparison of normalised COD: (a) SR data; (b) HR data (every fifth data point is shown).